Theses and Dissertations   Student Graduate Works

3-14-2014

Utilizing Near-IR Tunable Laser Absorption Spectroscopy to Study Detonation and Combustion Systems

Christopher J. McGahan

Follow this and additional works at: https://scholar.afit.edu/etd

Part of the Plasma and Beam Physics Commons

UTILIZING NEAR-IR TUNABLE LASER ABSORPTION SPECTROSCOPY TO STUDY DETONATION AND COMBUSTION SYSTEMS

THESIS

Christopher J. McGahan, Second Lieutenant, USAF

AFIT-ENP-14-M-22

DEPARTMENT OF THE AIR FORCE
AIR UNIVERSITY

AIR FORCE INSTITUTE OF TECHNOLOGY

Wright-Patterson Air Force Base, Ohio

UTILIZING NEAR-IR TUNABLE LASER ABSORPTION SPECTROSCOPY TO
STUDY DETONATION AND COMBUSTION SYSTEMS

THESIS

Presented to the Faculty

Department of Physics

Graduate School of Engineering and Management

Air Force Institute of Technology

Air University

Air Education and Training Command

in Partial Fulfillment of the Requirements for the

Degree of Master of Science in Applied Physics

Christopher J. McGahan, B.S. PHY & B.S. AERO

Second Lieutenant, USAF

March 2014

AFIT-ENP-14-M-22

UTILIZING NEAR-IR TUNABLE LASER ABSORPTION SPECTROSCOPY TO
STUDY DETONATION AND COMBUSTION SYSTEMS

Christopher J. McGahan, B.S. PHY & B.S. AERO
Second Lieutenant, USAF

Approved:

//signed//	13 March 2014
Col. Brian A. Tom, PhD (Chairman)	Date
//signed//	17 March 2014
Dr. Glen P. Perram , (Member)	Date
//signed//	13 March 2014
Dr. Andrew Caswell, (Member)	Date

Abstract

A Hencken burner, Rotating Detonation Engine (RDE), and a detonation tube were studied using a Time-Devision Multiplexed Tunable Diode Laser Absorption Spectroscopy (TDM-TDLAS) system to measure water absorption features over two spectral regions (7,435 to 7,442 cm^{-1} and 7,465 to 7,471 cm^{-1}) near 1.3 μm. These absorption features were fit with simulated spectra using data from the HITEMP database to obtain temperatures and water concentrations for the three systems. Velocity was calculated for the RDE system using the Doppler shift of the spectral lines. To perform the calculations necessary to obtain these results (temperature, concentration, and velocity) a Graphical User Interface (GUI) was developed with supporting code. A Hencken burner flame was studied at three different heights above the burner surface, for two different fuels; ethylene (C_2H_4) and methane (CH_4), both at various equivalence ratios. The C_2H_4 Hencken burner temperatures matched fairly well with the adiabatic temperatures once edge effects were taken into account, however, the CH_4 flame did not match as well. The exhaust of the RDE was studied at various equivalence ratios using a hydrogen-air mixture (H_2-air). The exhaust temperatures were found to linearly increase with equivalence ratio, from 1,300 K ($\phi \approx 1$) to 1,500 K ($\phi \approx 1.4$) and fluctuated with a standard deviation of approximately 50 K. The exhaust velocities of the RDE were found to be independent of equivalence ratio with an average value of 360 m/s and a standard deviation of 50 m/s. A detonation tube was studied at various equivalence ratios and initial pressures, also using an H_2-air mixture. Preliminary results are presented for the detonation tube, however, further work in that area is required.

Acknowledgments

This research would not have been possible without the help and support of many individuals. First and foremost, I would like to thank Dr. Andrew Caswell, for the use of his spectroscopic system, his time, and his vast knowledge in the field of spectroscopy. Without his patience, detailed explanations, and guidance, this research project would not have been possible. I would also like to thank my research advisor, Col Brian Tom, who's extreme patience, guidance, enthusiasm, and encouragement to improve the quality of this research was invaluable. I would also like to thank all of the people in D-bay who allowed me to use their tools, test rooms, and their technical knowledge to make the experiments possible. I am grateful for everyones time and effort for which this acknowledgment falls short of expressing.

Christopher J. McGahan

<div align="center">**Table of Contents**</div>

List of Figures

x

List of Tables

List of Symbols

Symbol	Definition
#*prod.*	total number of product species
#*react.*	total number of reactant species
a_1	intensity offset from light other than from the laser
a_2	intensity offset from light other than from the laser
c	speed of light [cm/s]
C	experimentally determined parameter for spectral feature selection
c_2	second radiation constant ($c_2 = {}^{hc}/_k$) [cm K]
$\bar{c}_{p,i}$	constant pressure specific heat for the ith species [J k/mole]
$Data_i$	i^{th} data point of the measured spectrum
E''	lower state energy of transition [cm^{-1}]
E_0	semiconductor bang gap energy at absolute zero [eV]
E_g	semiconductor band gap energy [eV]
G	Gibbs function
$g_G(v - v_0)$	Gaussian lineshape as a function of frequency and line center [cm]
g_i	degeneracy of the ith state
$g_L(v - v_0)$	Lorentzian lineshape as a function of frequency and line center [cm]
$g_{Voigt}(v, v_0)$	Voigt lineshape function [cm]
h	Plank's constant [J s]
H_{prod}	total enthalpy of the products [J]
H_{react}	total enthalpy of the reactants [J]
$\bar{h}_{f,i}$	total partition function
I	intensity of laser incident upon a detector [arbitrary]
I_0	initial laser intensity [arbitrary]

Symbol	Definition
I_{sim}	simulated spectrum [cm^{-1}]
k	Boltzmann's constant [cm^{-1}/K]
l	path length of the laser [cm]
LeftValley	intensity of the first valley to the left of the location of Peak [cm^{-1}]
M	unified atomic mass unit [amu]
n	coefficient of temperature dependence for pressure broadening
N	total number of particles in the system
N_c	total number of collisional partners
N_{H_2O}	water concentration [moles/cm^3]
N_i	number of moles of the ith species [moles]
N_i	population of the ith state
N_{pts}	number of data points in a measured spectrum
N_s	total number of complete scans for a certain channel
n_{air}	coeff. of temperature dependence for pressure broadening for air
n_i	coeff. of temperature dependence for pressure broadening for the ith species
P_{air}	partial pressure of air [atm]
Peak	intensity of the spectral feature being examined [cm^{-1}]
P_{H_2O}	partial pressure of H$_2$O [atm]
P_i	partial pressure of the ith species [atm]
P_{total}	total pressure of the system [atm]
Q	total partition function
R	ideal gas constant [cm^{3}atm/(moles K)]
Ref.Peak	intensity of the smallest peak in a particular laser scan [cm^{-1}]
RightValley	intensity of the first valley to the right of the location of Peak [cm^{-1}]
RMSE	root mean square error

Symbol	Definition
S	entropy of the system
S	spectral line strength $\left[\frac{\text{cm}^{-1}}{\text{molecule x cm}^{-2}}\right]$
Slope	slope of the line of best fit
T	temperature [K]
T_0	reference temperature [296 K]
T_{ad}	adiabatic temperature [K]
$x_{\text{H}_2)}$	mole fraction of water
y_i	i^{th} point in the line of best fit
α	experimentally determined constant for a semiconductor [eV/K]
α	absorption coefficient [cm^{-1}]
α_2	absorption coefficient without the intensity offsets removed [cm^{-1}]
α_{ave}	average absorption coefficient [cm^{-1}]
β	experimentally determined constant for a semiconductor [K]
$\Delta \nu_L$	FWHM of Lorentzian lineshape [cm^{-1}]
$\Delta \nu_G$	FWHM of Gaussian lineshape [cm^{-1}]
ε_i	energy of the ith state [cm^{-1}]
$\gamma_i(T_0)$	pressure broadening coefficient (HWHM) for the ith species at T_0 [cm^{-1}/atm]
ν	frequency in wavenumbers [cm^{-1}]
ν_0	line center frequency in wavenumbers [cm^{-1}]
θ	Debye temperature [K]

List of Acronyms

Acronym	Definition
AFIT	Air Force Institute of Technology
AFRL	Air Force Research Laboratory
BOA	Booster Optical Amplifier
CEA	Chemical Equilibrium with Applications
FSR	Free Spectral Range
FWHM	Full Width at Half Maximum
GUI	Graphical User Interface
LDC	Laser Diode Controller
MZI	Mach Zehnder Interferometer
NRL	Naval Research Laboratory
RDE	Rotating Detonation Engine
RMS	Root Mean Square
RMSE	Root Mean Square Error
TC	Temperature Controller
TEC	Thermal Electric Cooler
TDLAS	Tunable Diode Laser Absorption Spectroscopy
TDM-TDLAS	Time-Devision Multiplexed Tunable Diode Laser Absorption Spectroscopy
VCSEL	Vertical Cavity Surface Emitting Laser
ZND	Zeldovich, von Neumann, and Döring

UTILIZING NEAR-IR TUNABLE LASER ABSORPTION SPECTROSCOPY TO STUDY DETONATION AND COMBUSTION SYSTEMS

I. Introduction

Time Division Multiplexed Tunable Diode Laser Absorption Spectroscopy
(TDM-TDLAS) was used to measure water absorption features through the flame
of a Hencken burner, in the exhaust of an RDE, and in a detonation tube. The
TDM-TDLAS system used two lasers to scan over approximately 1 nm wavelength
ranges, near 1.3 μm. Even though water has very weak absorptivity in this region,
this spectral region was used primarily for two reasons. First, 1.3 μm fiber optics
were developed by the telecommunications industry in the 1980's and thus are readily
available, of good quality, and cheap. Second, spectral features from other atoms and
molecules are negligible in this region.

The spectroscopic system used time division multiplexing which allowed both
lasers to travel the same optical paths. While the lasers shared the same fibers they did
not share them at the same time, they alternated back and forth (time division). The
system was completely fiber coupled with the exception of where the lasers traversed
the medium being studied (i.e. the flame in the Hencken burner). The optical fiber
containing both lasers was split multiple times so multiple measurements could be
performed simultaneously.

The TDM-TDLAS system provided raw data, but an analysis of the data was
required to obtain useful information. Not only was the Beer-Lambert law utilized
to convert the spectral data into absorption profiles, corrections to the data had to be
made to account for experimental variations. These variations included, varying scan

speeds of the laser, a jitter in the spectral range scanned, and non-linear baselines. Additionally, individual laser scans had to be separated from each other, and the spectra had to be placed on a correct wavenumber axis. A GUI was developed in MATLAB to allow users to process raw TDM-TDLAS data, and to view the results along with the data at various stages of processing. Similar code existed for this system in LABVIEW, however to gain insight into how and what needed to be done to process the data, the new GUI was created in an attempt to provide faster ways to solve the problem.

A MATLAB code was used to analyze the data collected from the three different combustion/detonation systems studied. The first system, a Hencken burner, provided a stable flame in a controlled environment near adiabatic conditions. This flame was used to validate the techniques used to obtain temperatures for the RDE measurements as well as to provide data on flame temperatures at various heights above the burner surface and at different equivalence ratios for two different fuels. On the second system, the detonation tube, spectroscopic measurements were taken at various equivalence ratios and initial pressures. This data was used to show the difficulties in extracting temperatures from high temperature and pressure environments. The final system studied was the RDE. The exhaust of this system was studied over a range of equivalence ratios.

II. Background

2.1   Rotating Detonation Engines

2.1.1   *Previous* & *Current Research.*

RDE's have been and are currently being studied by various groups. At the U.S. Naval Research Laboratory (NRL) Schewer *et al.* have been studying RDE's under different operating conditions and developing simulations for them [14]. This research was presented in a review article in 2011 and they were able to show, with simulations, that the RDE has the potential to be considerably more efficient than current combustors [14]. The Navy continues to do research in this area.

At the Air Force Research Laboratory (AFRL) Naples *et al.* are working to further understand the RDE system. They have modified an RDE such that there is optical access to the flow field during operation, shown in Figure 2.1. With this optical access, chemiluminescence and shadowgraph measurements will be taken and used to characterize the flow field inside the RDE [9].

Figure 2.1: RDE with quartz outer body to allow visualization of the flow field inside of the RDE [9].

The systems used for most research are not designed to run continuously. They run for approximately 1 second, and then shut off. This is enough time to take measurements, however, this does not provide enough time for the system to come to thermal equilibrium. Without a cooling system the RDE would melt before thermal equilibrium was reached. That is why there is continuing research being done on

developing a cooling system. Figure 2.2 shows the RDE designed with water cooling channels through the outer body. This RDE was designed and tested by Theruerkauf for his thesis with the Air Force Institute of Technology (AFIT) and AFRL [16]. The thesis was completed, however, there is still ongoing research on this project.
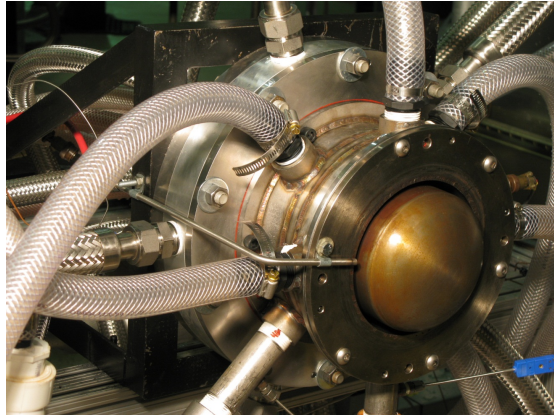
Figure 2.2: RDE with a water cooled outer body. The tubes coming out of the outer body in the front are for the water cooling. The ones in the back behind the outer body are for the fuel and oxidizer [16].

2.2 Spectroscopy

Spectroscopy is at the center of this research as it is for countless other research areas. It is a rapidly developing field, and was greatly expanded with the invention of the laser. Some of the past and present research relating to this thesis are mentioned below.

2.2.1 Previous Research.

In 2009, at the University of Central Florida, Saptarshi Basu used a Tunable Diode Laser Absorption Spectroscopy (TDLAS) system along with a laser modulated at a high frequency to measure the species concentrations of water vapor and carbon dioxide at both 12 cm and 12 mm path lengths with results repeatable within 10%

[1]. These path lengths are similar to those encountered in this research. In 2012 R.K. Hanson published a paper on measuring CO concentrations and temperatures for combustion gases in a shock tube [12]. While concentration measurements are not the goal of this research, Hanson's experiments were carried out in similar environments to the ones found in the systems which are analyzed in this study.

Recently at AFRL Caswell *et al.* used the same spectroscopic system as used in this research to measure multiple gas parameters in a pulsed detonation combustor (PDC) [3]. With this setup, gas temperature, pressure, H_2O mole fraction, and velocity were obtained. These results help validate the method and setup for this research. Additionally Caswell with Whitney used this system to take some measurements on an RDE [20]

2.2.2 Current Research.

At AFRL and the Air Force Institute of Technology (AFIT) Wakefield *et al.* are working on developing and utilizing a new TDLAS system which scans across absorption peaks of CO and CO_2 near 4.3 μm. This wavelength is used because of the negligible water absorption near that wavelength, so the primary absorption is from CO and CO_2. This system will help determine combustion efficiencies of difference detonation and combustion processes.

III.   Spectroscopy & The Spectroscopic System

3.1   Tunable Diode Laser Absorption Spectroscopy

Spectroscopy is the study of the interactions between light and matter. There are many different spectroscopic techniques. TDM-TDLAS was the technique used in this work. In this technique diode lasers are tuned to different wavelengths by changing the temperature of the diode. This was accomplished by increasing (ramping) the current to the diode which caused Joule heating, also known as resistive heating, resulting in rapid increases in temperature. The temperature was then more slowly brought back down using a Thermal Electric Cooler (TEC). This allowed for the laser to be tuned repeatably over the same wavelengths relatively quickly (the system used scanned at 10 kilohertz). Two Vertical Cavity Surface Emitting Laser (VCSEL) diodes were used. They were time-division multiplexed, meaning the lasers were alternated between being on and off. This was done to allow two different spectral regions to be interrogated without having to scan over a large range of wavelengths. Additionally, it allowed the lasers to share the same fiber optics (if they were on at the same time it would be very difficult to separate the signals to obtain meaningful data).

The current ramp also changed the intensity of the laser with wavelength (increasing the current to a laser diode increases the intensity of the output laser). This would mean that the intensity of the light incident on the detector would change with wavelength. This was not desired and was corrected for, and is discussed in section 3.3. Responsivity of photo-detectors is wavelength dependent, however, because the spectral ranges that were studied were small (≈ 1 nm) the responsivity of the InGaAs detectors was very constant.

Diode lasers can be tuned with temperature because they are made out of semiconductors. The wavelength of light emitted by the diode laser is inversely

6

proportional to the band gap energy of the semiconductor. According to the Varshni equation [18],

$$E_g = E_0 - \frac{\alpha T^2}{T + \beta},$$ (3.1)

the energy (E_g) of the band gap decreases with temperature (T) squared, α and β are experimentally obtained constants, and E_0 is the band gap energy at absolute zero. This relation is valid for $T < \theta/10$, where θ is the Debye temperature. For temperatures greater than this, the energy decreases linearly with temperature [18].

In tunable diode laser absorption spectroscopy the laser is tuned over a range of wavelengths and propagated through a sample to a detector at the other end. The output signal of the detector corresponds to the intensity of light incident upon it. This detected intensity is then compared to its initial intensity using the Beer-Lambert Law,

$$I = I_o e^{-\alpha l},$$ (3.2)

where I is the intensity of the light after it has passed through the sample, I_o is the initial intensity of the light, and α is the absorption coefficient and l is the path length of the laser through the test section. Solving Equation 3.2 for the absorption coefficient yields,

$$\alpha = -\frac{1}{l} ln\left(\frac{I}{I_o}\right).$$ (3.3)

When the intensities are obtained experimentally by scanning the laser over a range of wavelengths, the absorption coefficient in Equation 3.3 becomes a function of wavelength. Plotting this variable versus wavelength yields an absorption spectrum. The spectral features result from dips in the intensity (I) at certain wavelengths. These dips become peaks when the negative natural log is taken. These intensity dips arise from the fact that the energy levels of atoms and molecules are quantized so only the wavelengths that correspond to the available energy states of the atoms and molecules in the sample can be absorbed.

7

Every type of atom and molecule has its own distinct set of energy levels resulting in distinct absorption spectra. This can be used to identify atoms and molecules. The distinct energy levels change with temperature, pressure, and velocity (relative to the observer). The spectra at these different conditions can be simulated if the conditions are known at a reference temperature, pressure and velocity. These simulated spectra can then be used to determine the pressure, temperature, and velocity of a system if a measured spectrum is obtained.

At low enough temperatures, pressures, and with sensitive spectroscopic techniques, the spectral features can be resolved such that each individual absorption feature is distinguishable. Under these conditions a Voigt lineshape function can be fit to the data and using theory the temperature and pressure could be obtained.

Under normal pressures and temperatures the spectral features (due to perturbations in their energy states) are broadened such that it is impossible to distinguish individual transitions. This makes fitting the data to one Voigt function meaningless, because the broadened features are now made up of many different transitions. To obtain the temperature and pressure under these conditions the line positions must be obtained from a database such as HITRAN or HITEMP, and then a region of the spectrum must be fit with a simulation, as opposed to individual transitions. The temperature and pressure that produces a model that best fits the spectral data corresponds to the temperature and pressure of the sample being studied. There are limitations to this method which will be discussed in section 3.2.5.

3.2   Simulating The Spectrum

To simulate an absorption spectrum it is necessary to know the line intensities, lineshapes and how they scale with temperature and pressure. The simulated absorption spectrum can be represented by,

$$I_{sim} = S(T)g_{Voigt}(\nu, \nu_0), \tag{3.4}$$

where I_{sim} is the simulated spectrum, $S(T)$ is the line intensity as a function of temperature, and $g_{Voigt}(\nu, \nu_0)$ is the lineshape function as a function of wavenumber ν and the line center wavenumber ν_0. The lineshape function accounts for the broadening of the lines, primarily due to temperature and pressure.

3.2.1 Line Intensities.

The line intensities depend on temperature and they follow a Boltzmann's distribution. The intensities can be represented with relation to a reference intensity as [7],

$$S(T) = \frac{S(T_0)Q(T_0)}{Q(T)} \frac{\exp\left(-c_2\frac{E''}{T}\right) \left[1 - \exp\left(-c_2\frac{\nu_0}{T}\right)\right]}{\exp\left(-c_2\frac{E''}{T_0}\right) \left[1 - \exp\left(-c_2\frac{\nu_0}{T_0}\right)\right]}, \tag{3.5}$$

where $S(T)$ is the line intensity in ($\frac{cm^{-1}}{molecule \ x \ cm^{-2}}$), T_0 is the reference temperature (296 K), T is the simulated temperature, Q is the total partition function, ν_0 is the line center frequency of the spectral line (cm^{-1}), E'' is the lower state energy of the transition (in cm^{-1}) and c_2 is the second radiation constant, defined as $c_2 = {}^{hc}/k$, where h is Planks constant, c is the speed of light, and k is Boltzmann's constant.

The HITEMP database provides values for $S(T_0)$, E'', and ν_0. To find the values for the partition function the HITRAN website provides a Fortran code which calculates the partition functions at given temperatures using theoretically and experimentally derived equations.

3.2.2 Lineshape.

As mentioned in section 3.1, the Voigt lineshape function can be used to model spectral features. The Voigt function is the convolution of the Gaussian lineshape with a Lorentzian lineshape function. The necessity of using the Voigt function arises from the two primary line broadening mechanisms.

The first of these broadening mechanisms is collisional broadening, also known as pressure broadening. This type of broadening is homogeneous, and thus the spectral

9

features broadened by pressure can be modeled with the Lorentzian lineshape [2],

$$g_L(v - v_0) = \frac{\Delta v_L}{2\pi \left(\frac{1}{4}(\Delta v_L)^2 + (v - v_0)^2\right)},$$
(3.6)

where $g_L(v - v_0)$ is the lineshape, Δv_L is the Full Width at Half Maximum (FWHM) of the profile, v_0 is the center frequency of the absorption feature, and v is the frequency.

Pressure broadening arises from the collisions between atoms or molecules during radiative absorption or emission. During the collision of an atom or molecule with another atom or molecule the electric potentials interact, causing a perturbation of the energy states. If the atoms or molecules involved in the collision emit or absorb a photon during the collisional time period then this photon would have a different energy than the photon emitted or absorbed when the energy states were not perturbed [4]. This causes a broadening of the lineshape; as pressure increases collisions occur more frequently, and the higher the probably is that the photon absorbed will have a perturbed energy. Pressure broadening also has a temperature dependence. Changes in temperature are changes to the average velocity of the atoms and molecules, which alters the collision rate.

The FWHM (Δv_L) is needed for Equation 3.6. The FWHM is pressure, temperature, and collisional partner dependent. Working from HITRAN and Demtröder [4, 7] it can be seen that,

$$\Delta v_L(T, P) = 2 \sum_{i=1}^{N_c} \gamma_i(T_0) \left(\frac{T_0}{T}\right)^{n_i} P_i,$$
(3.7)

where the summation is over all of the collisional partners, N_c is the number of collisional partners, $\gamma_i(T_0)$ is the pressure broadening coefficient at half width at half maximum for the ith collisional species at the reference temperature ($T_0 = 296$ K), the term $(T/T_0)^{-n_i}$ scales the coefficient with temperature [7], n_i is the coefficient of temperature dependence of the collisional partner. HITEMP provides the n values for air, and are dependent on the transition of interest. For H_2O, n varies widely and

is not well known. It is believed to have a mean value of 0.64 which can be used, alternatively the *n* values for air can be used [7]. The *n* values for air (n_{air}) were used in this research. P_i is the partial pressure of the ith collisional species. HITEMP provides two pressure broadening coefficients, one for self collisions (in this case H_2O), and one for collisions with air. Expanding Equation 3.7 for these two collisions yields,

$$\Delta\nu_L(T, P) = 2\gamma_{H_2O}(T_0)\left(\frac{T_0}{T}\right)^{n_{air}} P_{H_2O} + 2\gamma_{air}(T_0)\left(\frac{T_0}{T}\right)^{n_{air}} P_{air}. \tag{3.8}$$

Once $\Delta\nu_L(T, P)$ is determined the Lorentzian lineshape from Equation 3.6 can be computed.

The second line broadening mechanism is Doppler broadening. As its name implies it is caused by the Doppler effect. At any temperature above absolute zero, atoms and molecules are in motion. This motion causes absorbed or emitted light to be blue or red shifted relative to the atom or molecule in motion. Since the atoms and molecules move in different directions relative to the laser, a range of different frequencies can be absorbed by a given transition, causing a broadening in the acceptable energies for that transition. This type of broadening is inhomogeneous and can be modeled with the Gaussian lineshape function,

$$g_G(\nu - \nu_0) = \frac{2}{\Delta\nu_G}\sqrt{\frac{\ln(2)}{\pi}}e^{-4\ln(2)((\nu-\nu_0)/\Delta\nu_G)^2}, \tag{3.9}$$

where $g_G(\nu - \nu_0)$ is the Doppler broadened lineshape, $\Delta\nu_G$ is the FWHM, and ν and ν_0 are the same as defined before, the frequency and the line center frequency respectively. The FWHM is defined as [4],

$$\Delta\nu_G(T) = 7.16x10^{-7}\nu_0\sqrt{\frac{T}{M}}, \tag{3.10}$$

where M is the unified atomic mass unit (amu), T is temperature, and ν_0 is again the line center frequency.

11

3.2.3 Convolutions.

The lineshape due to Doppler broadening is inhomogeneous and the lineshape due to pressure broadening is homogeneous. Because these lineshapes are modeled by different functions the FWHM from each of them cannot simply be added and then used in a function which models the spectral features. When both of these types of broadenings are present the convolution of the two lineshape functions must be taken to produce the Voigt lineshape function to model the spectral features. The convolution is defined as,

$$g_L(\nu - \nu_0) * g_G(\nu - \nu_0) = g_{voigt}(\nu, \nu_0) = \int_{-\infty}^{\infty} g_L(\nu_0' - \nu_0)g_G(\nu - \nu_0')d\nu_0', \qquad (3.11)$$

where ν_0' is the frequency range the functions are being convolved over, ν_0 is line center, and ν represents the frequencies over which the function must be evaluated to obtain a complete Voigt profile. This is the formal definition of the convolution, however, to simulate a discrete spectrum the integral can be represented as a summation. Both functions being convolved approach zero fast enough that the bounds on the summation can be reasonably approximated as finite, resulting in,

$$g_{voigt}(\nu, \nu_0) = \sum_{\nu_0'=\nu_1}^{\nu_2} g_L(\nu_0' - \nu_0)g_G(\nu - \nu_0'), \qquad (3.12)$$

where it is important to make the bounds ν_1 and ν_2 large enough such that the majority of the two functions being convolved are within those bounds. Ideally all of both functions would be within those bounds, however both the Lorentzian and Gaussian functions only converge to zero at $\pm\infty$. Figure 3.1 illustrates the convolution of a Lorentzian with a Gaussian. The Gaussian is swept across the Lorentzian profile. The overlapping parts of the function are multiplied together, and the area under the product of these two curves is the value of the Voigt profile at the line center of the Gaussian. As the Gaussian moves across the Lorenzian the Voigt profile is constructed point by point.

12

In Figure 3.1 the shaded region is the area under the curve created by the multiplication of the regions of the Gaussian and Lorentzian which overlap (or have the same x-value). This area is the value of the Voigt function at the line center of the Gaussian, shown as the yellow point on the figures. The green curve is the Gaussian which is being swept in the direction of the arrow across the Lorentzian (red curve). The black curve is the Voigt profile. In Figure 3.1c the magenta curve is the Gaussian moved to the Lorentzian's line center to allow for a comparison between the shapes of the profiles. Both the Gaussian and Lorentzian have FWHM of 0.3 cm^{-1}, and the resulting Voigt profile from their convolution has an approximate full width half max of 1.0 cm^{-1}.

(a) Starting the convolution   (b) $1/4^{th}$ of the convolution   (c) Ending of the convolution
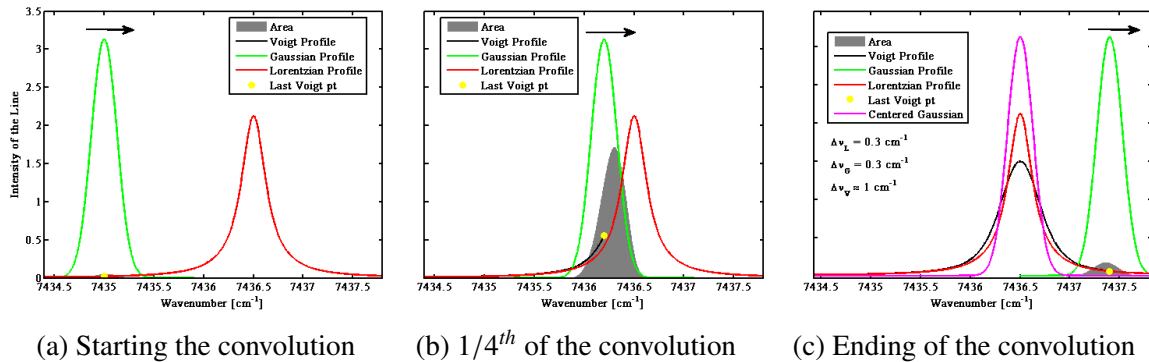
Figure 3.1: Convolution between a Gaussian ($\Delta\nu_G = 0.3$ cm^{-1}) and a Lorentzian ($\Delta\nu_L = 0.3$ cm^{-1}), resulting in a Voigt function ($\Delta\nu_V \approx 1.0$ cm^{-1}). The Gaussian is swept across the Lorentzian. As it travels the Gaussian and Lorentzian are multiplied together to create a new curve which is the outline of the shaded region. The area of that new curve, or the shaded region is the value of the Voigt function at line center of the sweeping Gaussian. In Figure (c) the Gaussian is overlaid at the Lorentzian line center. This was done to show a comparison between the three curves.

3.2.4 Validating the Method.

There are a large number of variables and equations that go into developing Equation 3.4, $I_{sim} = S(T) \, g_{voigt}(\nu, \nu_0)$, to simulate an absorption spectrum. This model is

by no means perfectly simulates a real spectrum and some of its shortcomings will be discussed in section 3.2.5. While it is not perfect, it is certainly useful, and its validity will be discussed.

There are a number of approximations that were made to use the numerical convolution discussed above. The first of these was already discussed. The function doing the convolving must approach zero in both directions fast enough such that the convolution does not have to be taken to $\pm$ infinity in order to yield a good approximation. In this research Gaussian spectral lines are convolved with Lorentzian lineshapes, which approach zero as $^1\!/_{x^2}$.

In order to convolve the Gaussian function with the Lorentzian, the Lorentzian function must remain constant during the convolution. In reality the Lorentzian FWHM is a function of line center. To avoid this problem, each individual Gaussian broadened spectral line could be convolved with its own Lorentzian function, however, this would be computationally expensive. Instead, as an approximation both spectral regions being studied were divided into four sections. Each section was convolved with its own Lorentzian profile. For the 1 nm spectral ranges being studied this was a good approximation. This approximation did not need to be made for the Gaussian profile, because it was computed completely with its defining equation, Equation 3.9.

To verify the validity of these approximations code was written to simulate the spectrum with a published empirical approximation to the Voigt profile developed by Whiting [19]. Figure 3.2 shows the spectral feature simulated with both methods which displayed the largest residual. The numerical simulation, used in this research, was plotted at every third point so both simulations can be seen. Whiting's method was reported as being within 5 percent in the worst case and normally within 3 percent of the actual Voigt profile. The maximum absolute difference between the two methods is 1.57 percent. This means in the worst case scenario the numerical approximation used

in the research is 6.57 percent from the actual Voigt profile, and in the best case it is 1.43 percent. This is acceptable because the Voigt profile is itself an approximation to the spectral features.
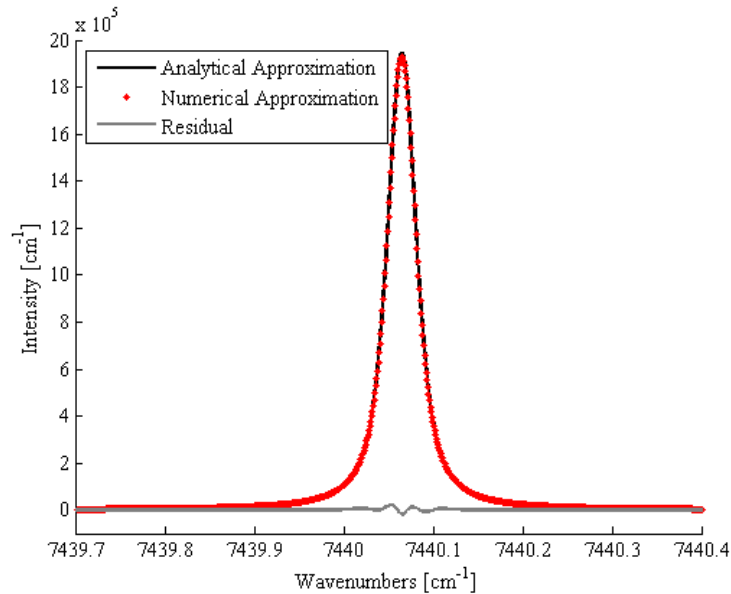
Figure 3.2: This figure depicts the validity of the approximations made for the numerical convolution. The spectral feature simulated with the convolution shows good agreement with Whiting's empirical approximation to Voigt profile. This spectral feature was chosen because it displayed the largest residual of the spectral lines being studied.

3.2.5 HITEMP Broadening Limitation & Fitting.

3.2.5.1 HITEMP Broadening Limitation.

The High-Resolution Transmission molecular absorption database (HITRAN) was designed to provide data to simulate the radiation in the atmosphere. The High-Temperature molecular spectroscopic database (HITEMP) is the same as the HITRAN database but with more spectral lines. A number of lines are removed from the HITRAN database because they are very weak at atmospheric temperatures. However some of these lines become the dominant lines at high temperatures. HITEMP preserves more of these lines.

15

The addition of lines makes HITEMP superior to HITRAN for higher temperatures, however, with all databases, the data is not perfect. Particularly, as mentioned before, the n value in Equation 3.8 is not well known for water. This is not a problem at atmospheric temperatures where the data in the database was primarily studied, however, at higher temperatures, like those found in flames, the values for the pressure broadening coefficient become very poor.

Figure 3.3 shows a spectrum, in blue, that was taken 5 mm above the Hencken burner, and two simulations of that spectrum. The temperature of the flame for this spectrum was calculated to be 1,580 K. The first simulation, shown in Figure 3.3a, was accomplished using HITEMP broadening coefficients. This method displays a large residual, with a resulting simulated temperature of 1,224 K.

The second simulation depicted in Figure 3.3b was calculated by letting the pressure broadening float to the best value. This method will be discussed in section 3.2.5.2. This resulted in a much better fit, as can be seen by the small residual. The temperature calculated using this simulation method was 1,575 K. Which agrees well with the calculated temperature.
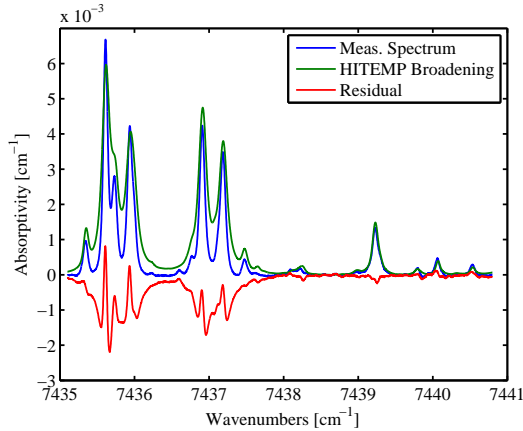
(a) HITEMP simulated data compared to measured data.
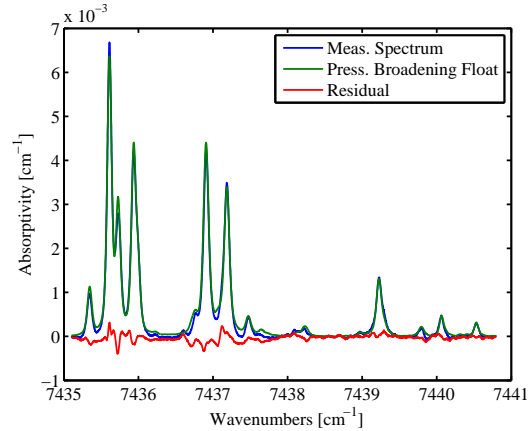
(b) Simulated data letting pressure broadening 'float' compared to measured data.

Figure 3.3: This figure shows the simulated data using both HITEMP broadening and letting the broadening float to the best value. The measured spectrum (shown in blue) was determined to be at 1,580 K using Dr. Caswell's code. The data was taken at 1 atm. The residuals show that letting the pressure broadening float produces a better simulation of the actual data.

3.2.5.2 Fitting Spectra.

Two minimization methods were used to find the simulated spectra which best fit the measured spectra, and were implemented in steps (b) and (c) in Figure 3.4. The first, a Golden Section search, was the more robust minimization method of the two, such that it always converged to a minimum value if one existed in the bounds being searched. However, it was slower than the second method, Parabolic Interpolation. The Parabolic Interpolation method was a much faster method, however, it was not guaranteed to converge. The code developed gave the user the option to pick either of the two methods, however, the parabolic method was designed such that if it did not converge it would automatically switch to the Golden Section search method.

Figure 3.4 shows the iterative process used to find the temperature and concentration while letting the pressure broadening float. To calculate the temperature

17

for a set of spectra (both the higher and lower energy laser scans) a temperature was initially guessed.

The guessed temperature (T_0 in Figure 3.4) was passed to the minimization routine chosen by the user. This routine found the pressure broadened FWHM ($\Delta \nu_L$) which minimized the error between the simulated spectra and the measured spectra for the given temperature by only adjusting the pressure broadening ((b) in Figure 3.4). This was accomplished by splitting both the higher and lower energy spectra into four sections. The best pressure broadening was found for each of these sections separately, all at the guessed temperature.

These 'best' pressure broadenings were then passed to a routine that used these values to find the temperature of the simulated spectra which minimized the error between the simulated spectra and the measured spectra by only adjusting the temperatures ((c) in Figure 3.4). This was accomplished by splicing together the higher and lower energy spectra to simulate both spectra at the same time. This could be done because both spectra were at the same temperature, and it was done to improve the temperature results.

The 'best' temperature was then compared to the temperature the pressure broadening was calculated with ((d) in the figure). If the absolute value of the difference between the newly calculated temperature and the one used for the pressure broadening was less than 1 K then the temperature was considered to be the temperature of the measured spectra. If the difference was greater than 1 K, the newly calculated temperature was used to find a new pressure broadening, and the process was repeated until the difference was less than 1 K.
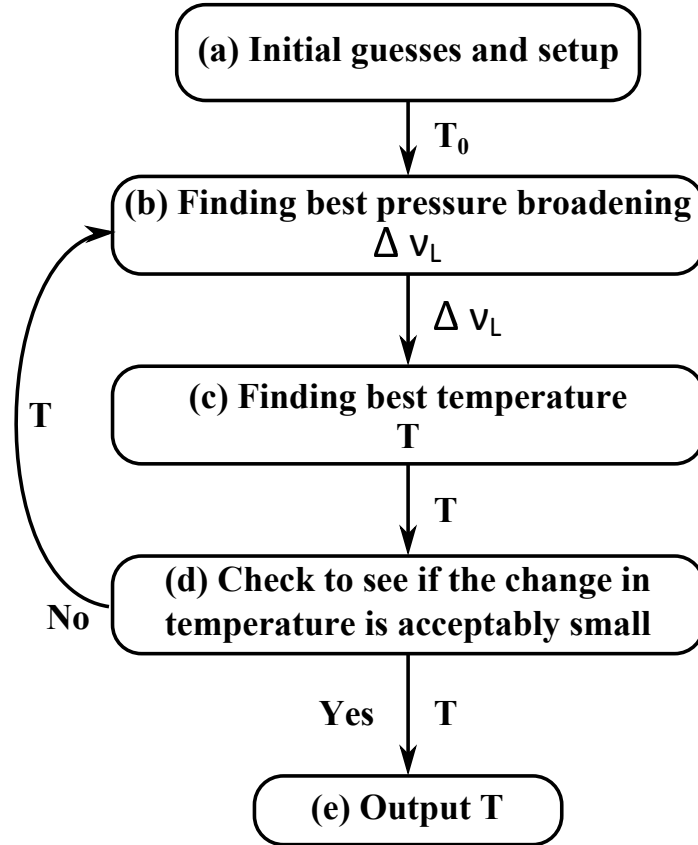
Figure 3.4: This figure shows the iterative process of finding the best temperature at the best pressure broadening which simulates the data. T_0 is the initial temperature, T is temperature of a particular iteration, and $\Delta\nu_L$ is the FHWM of the pressure broadening lineshape.

In the minimization routines used in (b) and (c) in Figure 3.4 a least squares approach was used to minimize the errors between the simulated and the measured spectra to find the best fit to the data. This was accomplished by minimizing the Root Mean Square Error (RMSE) of the difference between the measured data and the line of best fit of the curve created by the plot of the measured data versus the simulated data (Figure 3.5). The RMSE is given by,

$$\text{RMSE} = \sqrt{\sum_{i=1}^{N_{pts}} \frac{(y_i - Data_i)^2}{N_{pts}}}, \tag{3.13}$$

where y_i is the ith data point in the line of best fit, $Data_i$ is the ith data point of the measured spectrum, and N_{pts} represents the number of data points in the measured spectrum. Figure 3.5 shows line of best fit, y, of the measured data versus the simulated data.
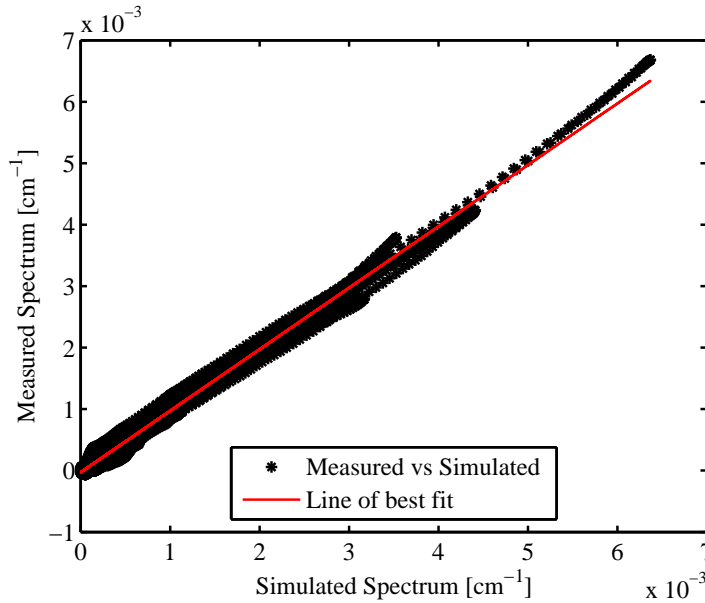
Figure 3.5: This figure shows a measured spectrum plotted against the best fit simulated spectrum, with the line of best fit. The simulated spectra was found such that the RMSE of the difference between the measured spectrum and the line of best fit was minimized. The RMSE error for this fit is 6.63e-5.

If the simulated data perfectly matched the measured data then the points in the figure would form a perfect line with slope 1 and an RMSE of zero. Figure 3.5 was partially created with the measured and simulated spectrum found in Figure 3.3b (it also includes the date from the higher energy scan), and has a RMSE of 6.63e-5, while the fit in 3.3a had an RMSE of 2.44e-4. The better the fit is the smaller the RMSE is, and the closer the simulated temperature is to the actual temperature of the medium being inspected. However, while in this case an RMSE of 2.44e-4 produced a bad temperature calculation (off by nearly 400 K) an RMSE of 2.44e-4 will not

20

always produce poor results. What constitutes a good value for the RMSE depends on the dataset. Higher levels of noise in the measured spectra can produce larger RMSE values, however, the spectral features may still be well fit by the simulation and thus produce a good estimate of the temperature. The RMSE value can also have a temperature dependence. At higher temperatures there were more spectral features in the regions of the spectrum being studied. The simulation may fit each of the features well, however, because there are more features at higher temperatures there will be a larger RMSE value.

There were two reasons the RMSE of the difference between the line of best fit and the measured data was used, as opposed to finding the RMSE of the residual of the measured and simulated spectra. The first reason was that minimizing the residual did not always result in the best fit between the measured spectra and simulated spectra. This resulted from two phenomena.

This first of these phenomena was that both the temperature and the pressure broadening had to be optimized. Because this was an iterative process (see Figure 3.4), sometimes in regions with small spectral features, the smallest residual occurred when the simulated spectrum simulated the baseline instead of the spectral features. This can happen when an iteration of the simulated temperature is inaccurate enough such that the simulated spectral features are significantly different than the measured spectral features.

The other phenomenon which caused this routine to not produce the best fit was due to an offset between the baselines of the simulated and measured data. When the baseline of the simulated spectrum and measured spectrum were shifted vertically from one another, minimizing the residual would force the simulated spectral features to be larger or smaller than they should have been to compensate for that shift.

The second reason the RMSE was found was to calculate the water concentration of the medium being studied. The concentration of water scales the intensity of the absorption features. This scaling has the effect of changing the slope of the best fit line. The slope was corrected to a slope of 1 by finding the slope of the best fit line, multiplying the simulated spectrum by that value, and then recalculating the best fit line using the correctly scaled simulated spectrum. The concentration was initially guessed using NASA's CEA code. This guessed value was then corrected by multiplying it with the slope, or scaling factor used to correct the simulated spectrum. The CEA code provides concentration in terms of mole fraction. To calculate the concentration of water in the sample, the following approach was used: First the partial pressure of water, $P_{\mathrm{H_2O}}$, was guessed using CEA,

$$P_{\mathrm{H_2O}} = x_{\mathrm{H_2O}} P_{total}, \tag{3.14}$$

where $x_{\mathrm{H_2O}}$ is the CEA value for the mole fraction of water at a given equivalence ratio, and P_{total} is the total pressure of the sample, which was assumed to be 1 atm. This could be assumed regardless of the pressure because of the scaling factor. Next the ideal gas law was used,

$$P_{\mathrm{H_2O}} = N_{\mathrm{H_2O}} RT, \tag{3.15}$$

where $N_{\mathrm{H_2O}}$ is the concentration of water in moles/cm^3, R is the ideal gas constant (82.06 cm^{3}atm/(moles K)), and T is the temperature in Kelvin. Equations 3.14 and 3.15 were solved for concentration,

$$N_{\mathrm{H_2O}} = \frac{x_{\mathrm{H_2O}} P_{total}}{RT}. \tag{3.16}$$

Finally the slope of the best fit line was found (before it was correct to 1), and $N_{\mathrm{H_2O}}$ was scaled with the slope, resulting in,

$$N_{\mathrm{H_2O}} = \frac{x_{\mathrm{H_2O}} P_{total}}{RT} * \mathrm{Slope}. \tag{3.17}$$

22

3.3 The TDM-TDLAS System

The spectral data analyzed in this research was collected using a Time Division Multiplexed Tunable Diode Laser Absorption Spectroscopy system (TDM-TDLAS) which was the first of three systems developed by Whitney *et al.*[20]. The system was completely fiber-coupled and the majority of it resided within a portable rack providing protection and mobility.

The system was fiber coupled to decrease the size of the system, increase it's mobility, increase it's durability (a free-space lens systems easily gets dirty and unaligned), and finally to increase the safety of the system by reducing the chance of laser induced injury.

Figure 3.6 shows a front view of the spectroscopic system. In the figure, (a.) shows the location of the computer which controlled the system and recorded the data. At (b.) eight ports can be seen (two of them have fibers connected to them) with green caps. Two of these lasers were used for reference intensities, the other six lasers could be used to take the spectroscopic data. The location of one of the temperature/laser diode controllers is shown at (c.).
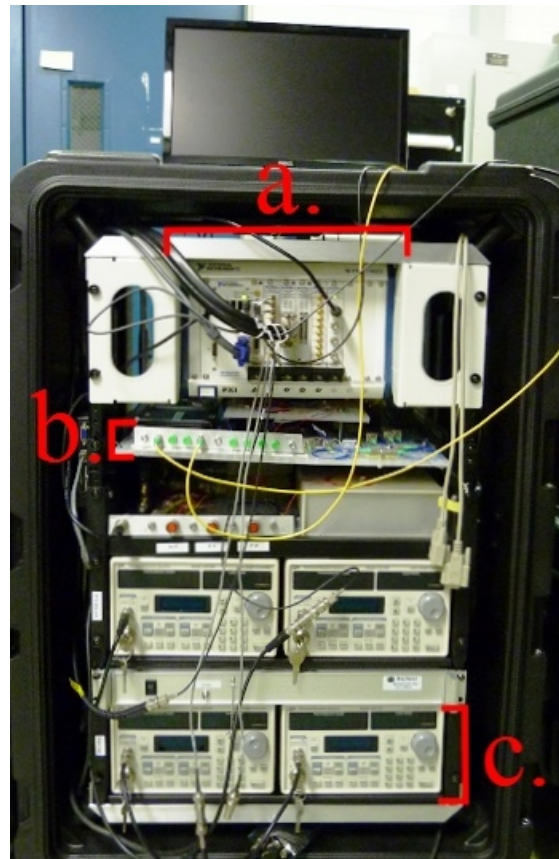

Figure 3.6: This is a front view of the TDM-TDLAS system. The controlling computer is shown at (a.). The eight laser output ports are shown at (b.), two of which have fibers attached to them. (c.) shows one of the four laser diode and temperature controllers.

Figure 3.7 shows a schematic of the spectroscopic system that was used in this research. The LabVIEW code was developed by Casewell which controls the Laser Diode Controllers (LDCs). This code provided the user with a range of controls. The primary controls allowed for the user to cycle power to the lasers, change the scan speeds of the laser by changing the current ramp, control the laser booster current ramp, view the laser signal live, and to take and save spectroscopic data. The lasers and the boosters were controlled by the computer through the LDCs, which are shown in both the picture of the device in Figure 3.6 and in the schematic in Figure 3.7.
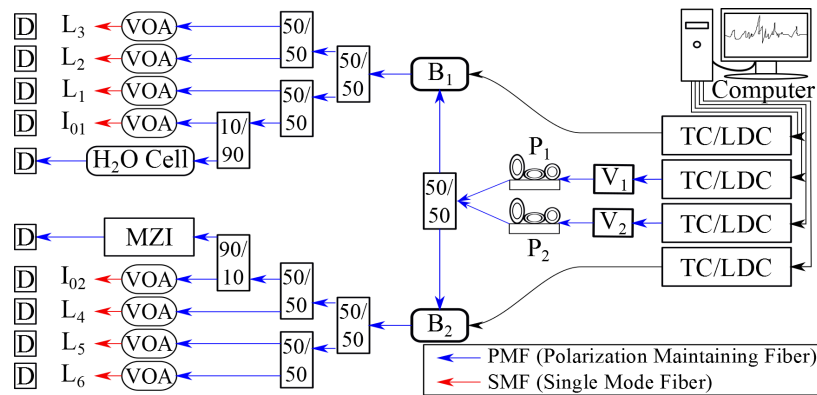

Figure 3.7: Depicted here is a schematic of the spectroscopic system. Moving from right to left; the TC/LDC is the temperature and laser diode controller, $V_{1,2}$ are the two laser diodes used, $P_{1,2}$ are polarizers, $B_{1,2}$ are booster optical amplifiers BOA's, the H_2O Cell, is the reference water cell held at 15 Torr, the MZI is the Mach-Zehnder Interferometer (MZI), the VOA's are variable optical attenuators, and the D's are photosensitive detectors (D). L_{1-6} are the lasers that are used to interrogate the sample under inspection and $I_{01,02}$ are the two laser beams used for reference intensities. After the sample light is collected by photosensitive detectors. The signals from the detectors go to the data acquisition (DAQ) boards on the computer. The rectangles containing fractions represent the split ratios. This picture was partially recreated from Reference [20].

The LDCs provided the current ramp from the code to the lasers and boosters. The Temperature Controller (TC) regulated the temperatures for both the boosters and the laser diodes by controlling a thermoelectric cooler. The temperature control was

slow compared to the rapid changes in temperature caused by the current ramps. The purpose of this was to allow the laser to heat up during the current ramp while still being able to cool down while the current ramp was off. The lasers were cooled so they could repeatedly scan over the same set of wavelengths.

To produce the laser beams, two vertical cavity surface emitting lasers (VCSEL's) were used, labeled V_1 and V_2 in Figure 3.7. They were driven by the LDC's, cooled by the TC's, and were alternated between scanning and being cooled. The two lasers were never on at the same time and they scanned over slightly different spectral ranges, $\approx$ 7,435 to 7,442 cm^{-1} and 7,465 to 7,471 cm^{-1}.

3.3.1   *Polarizers* & *Boosters*.

The signal from both laser diodes went through two polarization controllers (P_1 and P_2 in Figure 3.7). These polarizers were necessary because the BOA's (boosters) were sensitive to the polarization state of the lasers. After the polarizers the laser paths were combined and then split (50-50) to each of the BOA's. This was done so both lasers followed the same optical path through the rest of the system.

The BOA's (shown at B_1 and B_2 in Figure 3.7) were controlled by the TC and LDC in the same manner as the VCSEL's. The BOA's were used in two ways, the first was to boost the laser power. This was done by providing the laser with another gain medium to traverse. The second was to help correct for non-uniform laser intensities due to ramping the current (lasers increase in intensity with increased current). This was accomplished by calibrating the BOA's current ramp such that it compensated for the non-uniform intensity of the laser.

The signal from the BOA's was split multiple times, as shown in the figure. B_1 was split to go to the H_2O cell, reference intensity (I_{01}) and three output lasers for taking spectral data. The second booster (B_2) was split in a similar manner, but instead of the H_2O cell it went to a Mach-Zehnder Interferometer (MZI). With the exception

25

of the lasers to the H_2O cell and the MZI, the lasers passed through a variable optical attenuator (VOA), which was used for laser power adjustments.

The MZI data was used to convert the data collected in the time domain to a relative wavenumber axis and to correct for slight changes in the scanning rate of the laser. This was accomplished by using the inference pattern from the MZI along with the fact that one period of the interference pattern corresponded to the free spectral range of the laser.

The H_2O cell was used to obtain a reference spectrum with known conditions. This allowed the relative wavenumber axis obtained with the MZI to be converted into an absolute wavenumber axis by comparing absorption features using HITEMP data. The absorption coefficient was calculated with Beer's Law, using the reference laser intensities (I_0 in Figure 3.7) along with the signals from the interrogating laser, and the length of the laser beam path through the test medium.

IV. Data Processing

The data collected by the spectroscopic system required considerable manipulation before the fitting discussed in section 3.2.5.2 could be performed. The raw data collected was the electrical current response of the detector to the intensity of the light incident upon it. The following sections discuss the MATLAB GUI developed to process the raw data.

4.1 Whole Number of Scans

The spectroscopic system began taking data once it was triggered. The trigger event depended on the type of experiment being performed. For the Hencken burner experiment the system was triggered by one of the laser channels, and began taking data upon command. However, with experiments that were more time sensitive such as the RDE and detonation tube, the trigger was linked to the ignition of the detonation system. This allowed the event to be captured without having to take a large amount of data before the event started.

The trigger event determined when the data from the system started being saved. Independent of this event the lasers were scanned over their respective wavelength ranges. This was done to ensure the lasers were stable and already operational when the trigger event occurred. However, because the recording of data and the scanning of the lasers were not necessarily dependent on one another, a partial scan had a high probability of being recorded at the beginning and end of the data set. The system stopped taking data in one of two ways, either the system collected a specified quantity of data, or it acquired data for a specified amount of time. Figure 4.1 shows a small section of data where the system started taking data in the middle of a scan, as well as what a whole scan looks like. An assortment of other useful features are also shown.
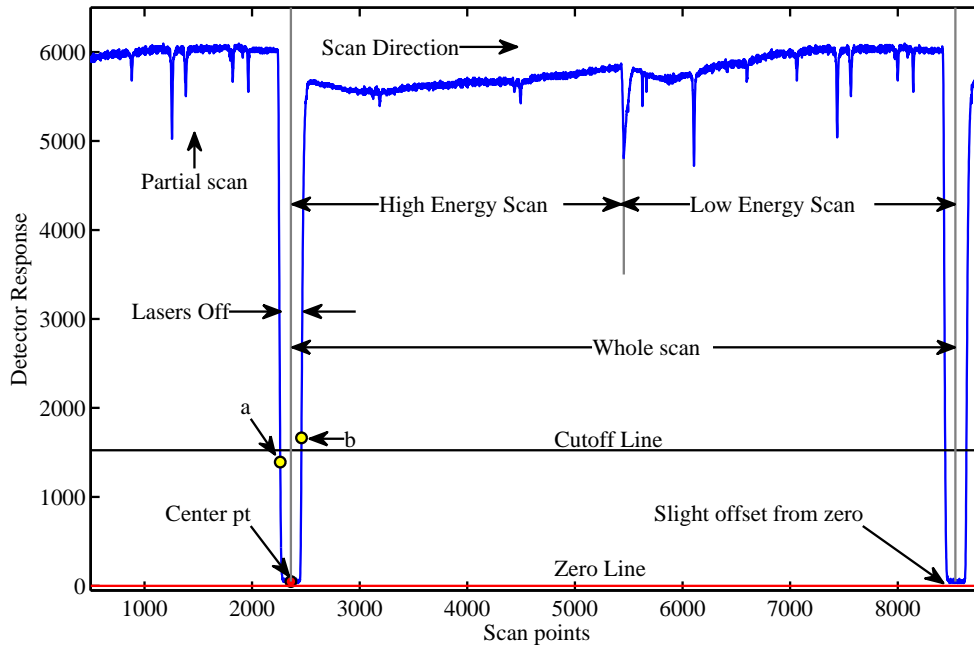
Figure 4.1: This is raw data taken from the water cell channel during one of the experiments. The yellow circles are the points used to determine the start of the first whole scan (red circle). They do not perfectly fall on the cutoff line, but are the closest points to it. The feature where the scan transitions from the high energy scan to the low energy scan is not a spectral feature, rather it is the result of the one laser turning off and the other laser turning on.

There are a few key reasons why it was important to remove the partial scans. To process the data, data from each of the lasers had to be separated and analyzed individually. Partial scans would make it difficult to separate the laser signals because the number of points in a partial scan were not known. Partial scans contained little useful data, therefore they were removed.

There were two partial scans for each of the different channels data was recorded on for every data set. Channels refer to the different ports on the data acquisition board. Each detector used in the experiments had its own channel. A data set refers to all

of the data recorded for all of the channels between a given trigger event and stop condition.

The data from the water cell was used to remove the partial scans at the beginning and end of the data from each of the channels. To accomplish this a cutoff criteria of $^1/_4{}^{th}$ of the maximum value of the water cell data was established. This cutoff value is shown in Figure 4.1 as the black horizontal line labeled as *Cuttoff Line*. Points below the cutoff value were regions where both lasers were off. Once this cutoff height was defined, the code found the first point (a) that was less than this cutoff and the first point (b) after point (a) that was greater than the cutoff value. If the first few points of the scan were below the cutoff value they were ignored and the next scan was examined. Ignoring the first few points was done to ensure a more robust removal of partial scans. Points (a) and (b) are shown as yellow circles in Figure 4.1. The average x-axis location of these two points was rounded down to give the approximate location of the center position shown as a red circle in the figure. The red circle shows the location where the first full scan started. The same method was applied to the end of the scans in reverse order.

4.2   Offset Correction

Figure 4.1 shows that during the period of both lasers being off there was a slight offset from zero. This resulted from the detector picking up ambient light. Due to the fact the water cell was completely fiber coupled, this offset most likely resulted from thermal noise in the detector (dark current). For the lasers not completely fiber coupled, such as the ones used to inspect the test medium, the offset was much larger and mostly came from the radiative emission of the experiment. The offset can be seen more clearly in Figure 4.2. This offset had to be removed otherwise it would result in an incorrect spectrum. This can be seen by examining Equation 3.3. Adding an offset

to the intensity terms results in,

$$\alpha_2 = -\frac{1}{l} ln \left(\frac{I + a_1}{I_o + a_2} \right),$$

(4.1)

where a_1 and a_2 are the intensity offsets. Equation 4.1 is only equivalent to Equation 3.3 if a_1 and a_2 are zero. Depending on the radiative emission of the experiment, the offset for the intensity could be comparable with the laser's intensity which would result in large discrepancies between the two equations.

To correct for this offset, points from the middle of the "laser off" periods were averaged for each of the scans. A line was then interpolated between these points and was subtracted from the data. This is depicted in Figure 4.2.
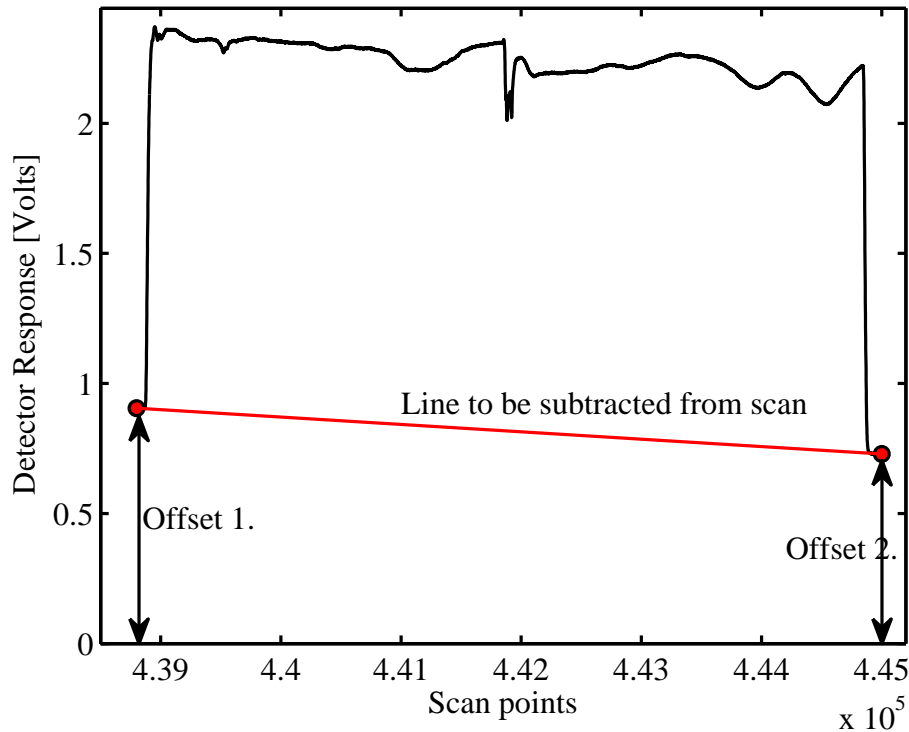
Figure 4.2: This figure clearly shows the offset which occurs to varying degrees depending on the experiment. This data was taken from one of the interrogating lasers from the detonation tube experiment. The red circles are located at the edges of this scan, which are the middles of the "laser off" period. They are the average values of these regions. The red line between them is the interpolated line which is subtracted from the data to remove the offset.

4.3 Separating the Scans

The system scans the higher energy laser first, making it the left laser scan in Figures 4.1 and 4.2. However, when the lasers were separated the order in which they were plotted was switched. This was done because the absorption spectra were plotted on a wavenumber axis and it is more intuitive to plot from low to high energy. This means the left scan in the raw data, once the scans are separated, is plotted on the right in this work. To avoid confusion individual lasers are referred to with low or high energies, as opposed to left or right scans.

To separate the laser scans the Root Mean Square (RMS) of the Mach Zehnder Interferometer (MZI) data was used. Figure 4.3 shows the RMS in red and one of the MZI scans in blue. The RMS was used because of the distinct change in signal between lasers when the lasers were on and when the laser were off. To determine where the laser turned on and off a cutoff criteria was created and is shown as the black line in the figure. This line was 80% of the mean value of the RMS. This value was chosen such that all of the data points for which the lasers were on were above the line, and the majority of the transition data points between the laser being on and off where below the line. To remove the transition points above the line, without risking the loss of the points for which the lasers were on, the second peak after the cutoff line from the end points was chosen as the start and stop points of the laser scans. The second peak from the end points are shown as yellow circles in Figure 4.3. The indices were found for the regions between the yellow circles for the low and high energy laser scans in the RMS data. These indices were then shifted for each of the scans and were applied to the data from all of the channels.
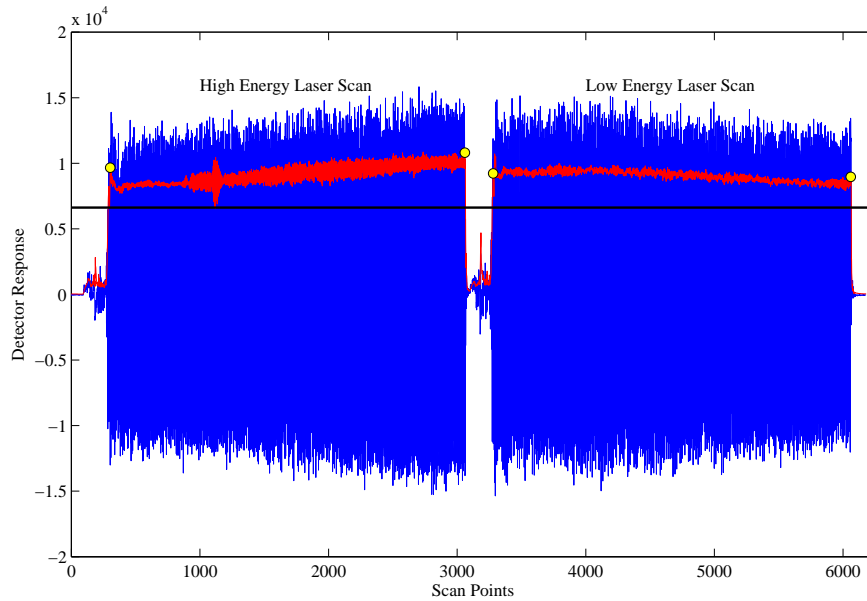
Figure 4.3: This figure shows the locations used to separate the data (yellow circles). The blue curve is the MZI data, and the red curve is the Root Mean Square of all the MZI scans. The RMS was used to separate the data because of the clear boundary between the laser being on and off. The black curve is the cutoff value used to help determine where the lasers turn on and off.

4.4 Variable Scan Speeds

Once the scans were separated into the individual laser scans a number of corrections had to be made to the data sets. The first of these was to correct for the inhomogeneous scan speeds of the laser. The changes in scan speed during a scan arose from the laser diode not being heated by the current ramp at a perfectly steady rate. This caused the line shapes in the spectrum to be artificially narrowed or broadened depending on whether the scan speed was faster or slower, respectively. The inhomogeneous scan speeds also resulted in spectral features being shifted non-uniformly throughout the spectrum. This happened because a non-uniform number of points were taken over a given amount of time. This meant that the data points were not evenly spaced in the time domain.

33

The MZI channel was used to correct for this non-uniform distribution of data points. The primary purpose of the MZI was to correct for these variations in scan speed. The peaks in the MZI data correspond to the maximums in intensity of the fringe patterns produced by the interferometer. The distance between fringe maximums correspond to the Free Spectral Range (FSR) of the laser for the MZI. The FSR of the higher energy laser was given as 460 MHz and for the lower energy laser it was 458 MHz. However, these values did not perfectly correct the spectra. Code was developed to recalculate these values. This was accomplished by finding the FSR which best shifted the locations of the water cell spectral lines to match the simulated HITRAN spectra. The data in the HITRAN database are very well known for the conditions of the water cell. The FSR values were found to be 458.26 MHz and 458.18 MHz for the lower and higher energy laser, respectively. This calculation only had to be performed once, because the FSR of the lasers was very constant.

Using the new FSR values, the frequency between data points was determined. Since the MZI data was collected simultaneously with all of the other channels, and with the same lasers, each data point in the MZI was in the same temporal location as the corresponding points in the other channels, so the adjustments found with the MZI channel could be applied to the other channels as well.

When the scan speeds of the laser changed so did the spacing of the fringes from the interferometer. Thus the MZI peaks changed as well. Figure 4.4 shows a close-up of the MZI data. The red squares correspond to zero crossings, which were used instead of the peaks, because the peaks were not well resolved. The distance between every other zero crossing was the same as the distance between adjacent peaks. The black stars and the magenta circles are the data points. As an example for how the MZI can fix the spacing between points consider the nine magenta points. They span three zero points, therefore the frequency difference between the first point and the last

point is approximately the FSR of the laser. This information can be used to create a new x-axis in the frequency domain by assigning each point between a set of three zero locations (red squares in the figure) representing some fraction of the FSR. If the first magenta point is considered the starting point, 0, then the second point would be located approximately at 57.5 MHz, and the third would be 115 MHz. This is continued until the third zero (red square) is reached. Thus the spacing between the next set of points spanning the next three zeros is calculated. This correctly spaces the points on a frequency axis.
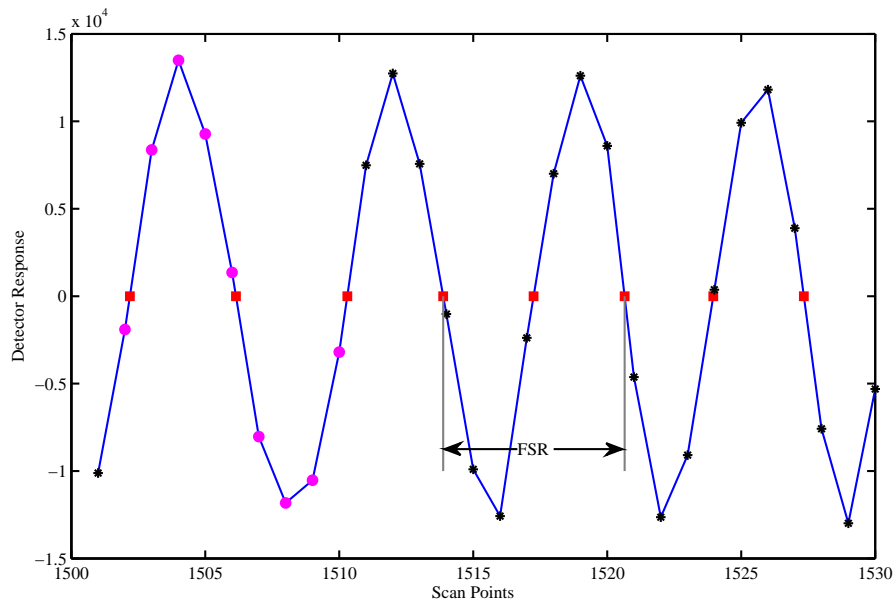

Figure 4.4: This is a close up of the MZI data. The distances between peaks, or between three zero crossings, corresponds to the FSR of the laser. The red squares show the inter-polated zero crossing. The black stars show the data points, and the magenta circles are used as an example of how this information can correct for scan speed variations.

4.5 Scan Range Jitter

Similar to the variable scan speeds, jitter in the scan range was related to the heating of the diode. Jitter in the scan range were slight variations in the spectral range

35

from one scan to the next. This was caused by not starting and stopping the scan of the laser diode at exactly the same temperature each time. This resulted in the spectra from each scan to be slightly shifted from each other. This jitter in the scan range had to be corrected for the cases for which multiple scans were averaged together. This correction was also applied to data that was not averaged to simplify the method used to put the spectra on an absolute wavenumber axis.

To correct for this, all of the spectra were placed on a relative wavenumber axis. This was accomplished by using the water cell channel. Since the water cell was kept at constant conditions, the spectral features did not change remarkably from scan to scan. The first water cell scan for each laser was chosen as a reference point upon which all other scans were based. The two lasers were handled individually. The maximum peak locations for every scan for both low and high energy laser were found and compared to the maximum location of the reference scan. Each scan was shifted by the difference between the maximum peak locations and the reference location. This aligned all of the scans on a relative axis. The significance of this can be seen in Figure 4.5. One hundred scans of an absorption feature from the water cell are shown in both (a) and (b). Figure 4.5a shows the features not corrected for the scan range jitter, and Figure 4.5b shows the data corrected. If the spectra were averaged without correcting for this jitter the features would be artificially broadened and reduced in magnitude, which would result in an incorrect fit with the simulated spectra.

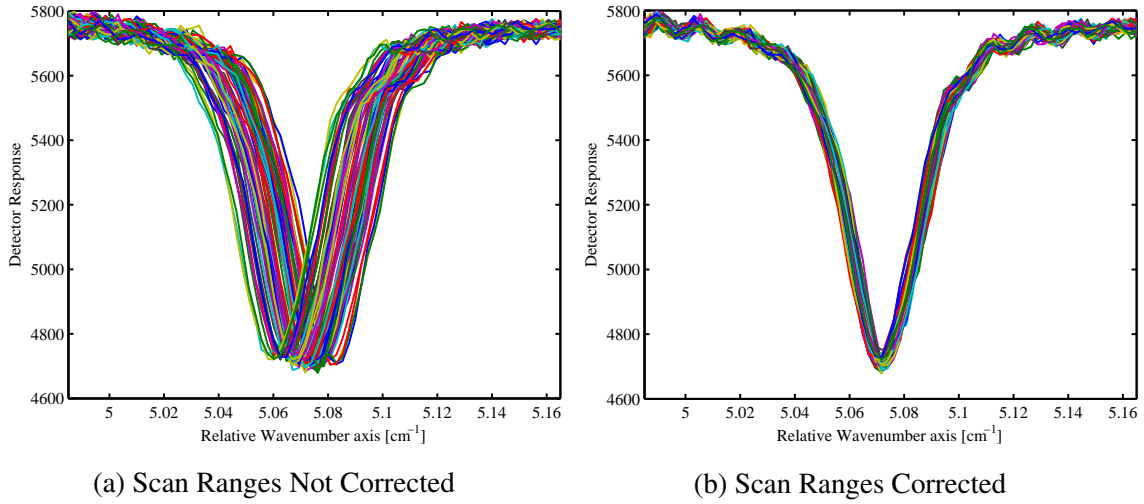(a) Scan Ranges Not Corrected

(b) Scan Ranges Corrected

Figure 4.5: These figures depict the significance in correcting for the slight changes in scan range from scan to scan. This data was taken from the water cell during one of the experiments of the lower energy laser.

4.6   Absorption Spectrum

The next step in manipulating the data was to convert the absorption features into absorption spectra. This was accomplished by applying Beer's Law to solve for the absorptivity coefficient as shown in Equation 3.3.

For the experiments in which the average of the spectra was taken, the absorption spectra was calculated prior to averaging. The reason the absorption features were not averaged before converting the spectral information into an absorption spectrum was because the average of the spectra was desired and not the spectrum of the averaged spectral information, that is,

$$\alpha_{ave\ 1} = -\frac{1}{lN_s} \sum_{i=1}^{N_s} \ln\left(\frac{I}{I_0}\right)_i, \tag{4.2}$$

was desired over,

$$\alpha_{ave\ 2} = -\frac{1}{l} \ln\left(\frac{\sum_{i=1}^{N_s} I_i}{\sum_{i=1}^{N_s} I_{0i}}\right), \tag{4.3}$$

where N_s is the total number of scans. Both equations yield similar results, however, they are not equivalent. Equation 4.2 is the average of the spectra, and Equation 4.3 is the spectra of the averaged spectral information (the N_s divided out). The temperature obtained from these averages would be different. Equation 4.2 was chosen over Equation 4.3 because the temperature of the averaged spectra more closely represents the actual temperature as opposed to the temperature from the spectrum of averaged spectral information. This results from the fact that in equation 4.3 the individual laser scans are not being divided by their corresponding reference intensities I_0. This means that variations that occur on a per scan basis that would normally be divided out by the same variations occurring in the reference intensity could no longer be divided out.

The averaged data can be used for steady state systems, like the Hencken burner and the RDE after startup. It loses meaning when applied to a system which changes over time like the detonation tube and the RDE. The reason the spectra were averaged was to reduce the noise to produce better results. When a system is not at a constant temperature the average of the spectral features collected over time will reduce the noise, but will also vastly change the spectral features. This is because the spectral features are a function of temperature.

4.7 Absolute Wavenumber Axis

To correct for the scan range jitter the scans were placed on a relative axis. This means that all of the scans would start with a wavenumber of zero and end at the spectral width of the scan. For data that had not been averaged, all of the spectra from a particular laser would be on that same relative axis. To fit a spectrum to the data, the absolute wavenumber axis must be known.

To accomplish this, the water cell data was used once again, in a similar fashion as it was before. The scans from each of the two lasers (low and high energy) from the water cell were averaged, resulting in two spectra, one for each laser. These spectral

features were then compared to HITRAN lines until a match was found. This was done by knowing approximately what range the lasers scanned over and then by looking in that region.

This process was not automated, however, it only had to be accomplished once to find the spectral range each laser scanned across; the range of the lasers did not change from experiment to experiment.

Once the range was found by hand, the code matched the maximum feature in the HITRAN database with the maximum feature from the averaged water cell spectrum for each laser. The difference in locations between these two peaks was used to shift all of the spectral information from each of the channels, and it was left as a default setting in the GUI.

4.8   Correcting the Baseline

Baseline correction was rather difficult, and was relatively important to do correctly. There were two methods used to correct the baseline in the code developed for this research. The method used was determined by user input. The baseline was created by a number of different phenomenon, such as irregularities in the laser diode as it scanned across the wavenumbers (the BOA's did not completely correct for these irregularities), by impurities in the optics, and by nonlinear changes in the radiative emission of the medium being studied which were not removed by the linear offset correction. Impurities in the optics can be from small particles of dust on the fiber ends, as well as impurities in the materials themselves.

4.8.1   Method 1.

The first method used to correct the baseline determined which features in the data were spectral features and which were from the noise and baseline. The features that were determined to be spectral features were ignored, and the remaining curve was assumed to be the baseline. A line going through the center of those remaining points

39

was subtracted from the spectrum with the features in it. At low pressures this baseline method was used to determine which features were spectral and which were not to a very high degree of success. Figure 4.6 shows a spectrum before and after the baseline correction was applied using this feature finding method.
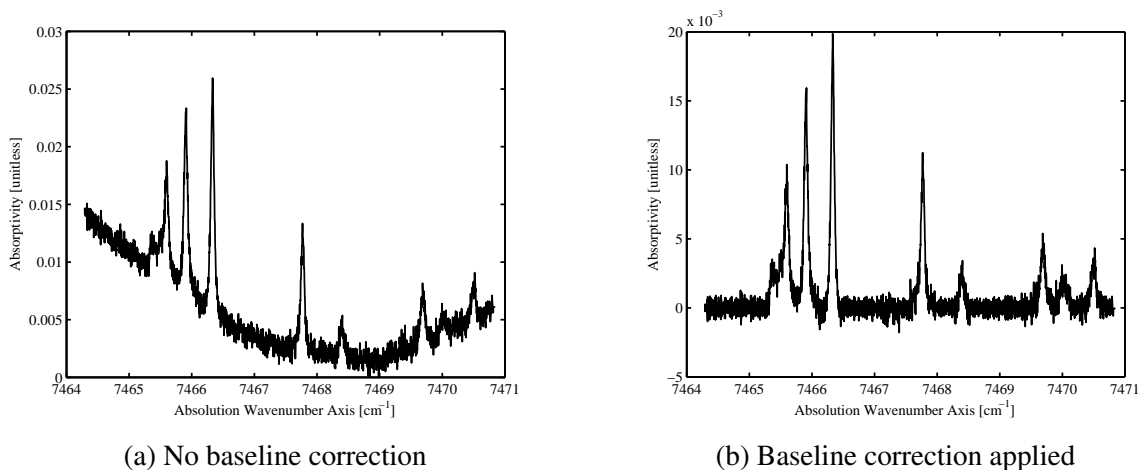

(a) No baseline correction   (b) Baseline correction applied

Figure 4.6: This figure illustrates how large of a difference there can be between a spectrum which has and has not had the baseline corrected. The data were taken during one of the Hencken burner experiments.

The first step was to make a linear baseline correction. This was done by creating a straight line that connected the end points of the data, and subtracting those values along that line from the spectral data. Next the data was smoothed considerably by convolving it with a Gaussian. This was done to remove the noise from the peaks. Then all of the peak and valley values were found (Figure 4.7). To determine which peaks were spectral features and which were not, each peak was compared to its two neighboring valleys. The relative difference between the peak and the two valleys, scaled by the smallest peak, was examined to determine which features were spectral and which were not. The peak was considered a spectral feature if the following statement was true;

$$\text{Spectral Feature} = C < \frac{\left|\text{Peak} - \text{Left Valley}\right|}{\text{Ref. Peak}} \quad \text{or} \quad \frac{\left|\text{Peak} - \text{Right Valley}\right|}{\text{Ref. Peak}} > C, \quad (4.4)$$

where Left Valley corresponds to the valley directly to the left of the peak being looked at, and Right Valley corresponds to the valley directly to the right of that peak, Peak was the intensity of the feature being examined, and Ref. Peak was the smallest peak intensity in that particular laser scan for which the baseline was being corrected. C was user input; a reasonable value for C, determined experimentally, was 0.005. The larger the C value the more restrictive the search was, increasing the number of features that were treated as noise. The reference peak was used to scale all of the differences by the same amount to correct for large changes in the baseline. Once the spectral peak locations were determined, the points between the two valleys straddling the peaks were found. These valleys are depicted by the cyan circles in Figure 4.7. The regions between the valleys were considered to be part of the spectral features and thus were not subtracted out.
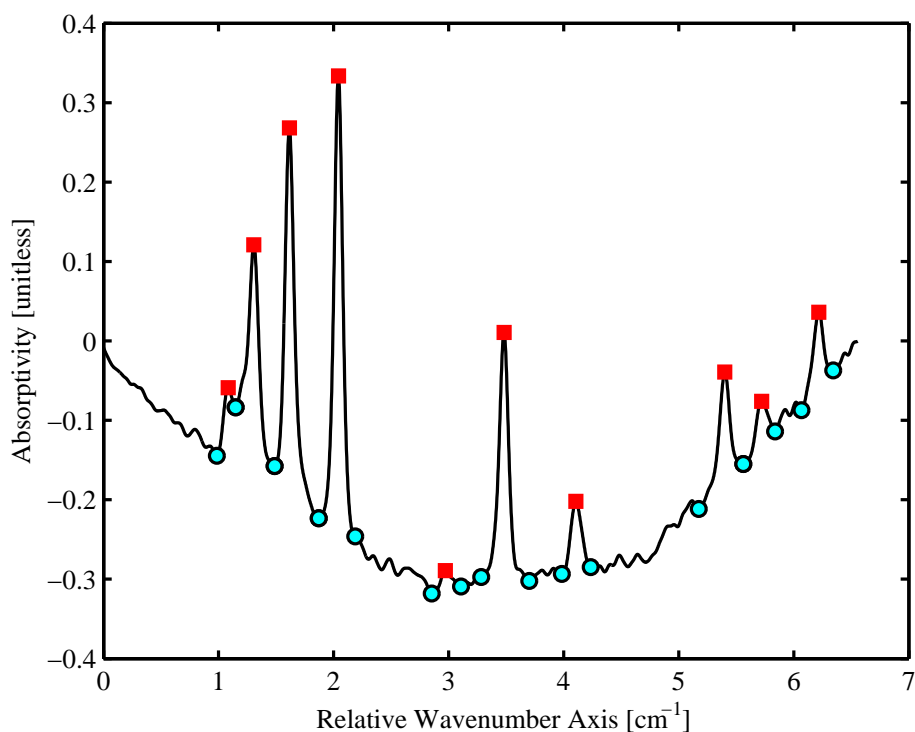
Figure 4.7: The spectrum shown here is not fully baseline corrected. The linear fit to the end points was already completed. The peaks are shown as red squares and the valleys for those peaks as cyan circles.

The locations of the spectral features found using the very smoothed spectrum (smoothed with a Gaussian with a FWHM of 0.01 cm^{-1}) were then temporarily removed from non-smoothed spectrum. The minimum and maximum locations were then found for this noisy spectrum which had the spectral features removed. The minimum and maximum locations were then linearly interpolated over the wavenumber positions for all the data points in the spectrum. The average of the two interpolations (of the mins and maxes) was considered to be the baseline and was subtracted from the non-smoothed spectrum.

This method worked well for normal pressures, with a moderate to large signal to noise level. This method was also useful for very unstable baselines. However, it ran

42

into problems with the high pressures found in the detonation tube. In high pressure environments the spectral lines were extremely broadened. Sometimes, when the above method was applied to high pressure spectra, the regions the method determined to be spectral features spanned the entire spectral range of the data. This was because it could not distinguish the baseline from the spectral features. In this case this baseline correction method would not alter the spectrum at all. Thus the baseline was not corrected.

This method also failed on spectrum with low noise levels. This happened because this method required enough noise left in the baseline in the smoothed spectrum to determine the valley locations. Another short coming of this method was the fact that there was no guarantee how much of the base of the spectral features would be preserved. This was a problem particularly for the smaller spectral features where the noise level made it so the chosen valley for a small spectral peak was on the feature instead of truly at the edge of the feature. This caused small features to be reduced in magnitude, and sometimes completely lost. The parameters could be adjusted to fix this, however, the sensitivity of this method for small features sometimes required the user parameters to be adjusted from scan to scan. This became impractical with the number of scans ranging in the thousands.

4.8.2   Method 2.

While Method 1 worked well under certain conditions, its short comings required the development of another method. The second method used an iterative method of fitting polynomials varying oder to the data.

First, the standard deviation of the noise level was found by determining the absolute minimum of the data and calculating the standard deviation for 25 points on both sides of the minimum. It was assumed that these values would not be part of a

spectral feature. This was a fairly good assumption, because it was unlikely a spectral feature would be that close to the minimum of the spectrum.

To improve convergence rate, all of the local minimum values were found. A low ordered polynomial was then fit to these minimums, usually a third order polynomial was sufficient. Ten times the standard deviation, mentioned above, was added to the low order polynomial. This is depicted in the Figure 4.8. The blue curve is the spectrum without any baseline corrections, the green line shows the low ordered polynomial fit to the local minimums of the spectrum, and the dashed red line shows ten standard deviations above the polynomial. Ten standard deviations were chosen to ensure that the only features above that value (the red dashed curve in the figure) were spectral features.
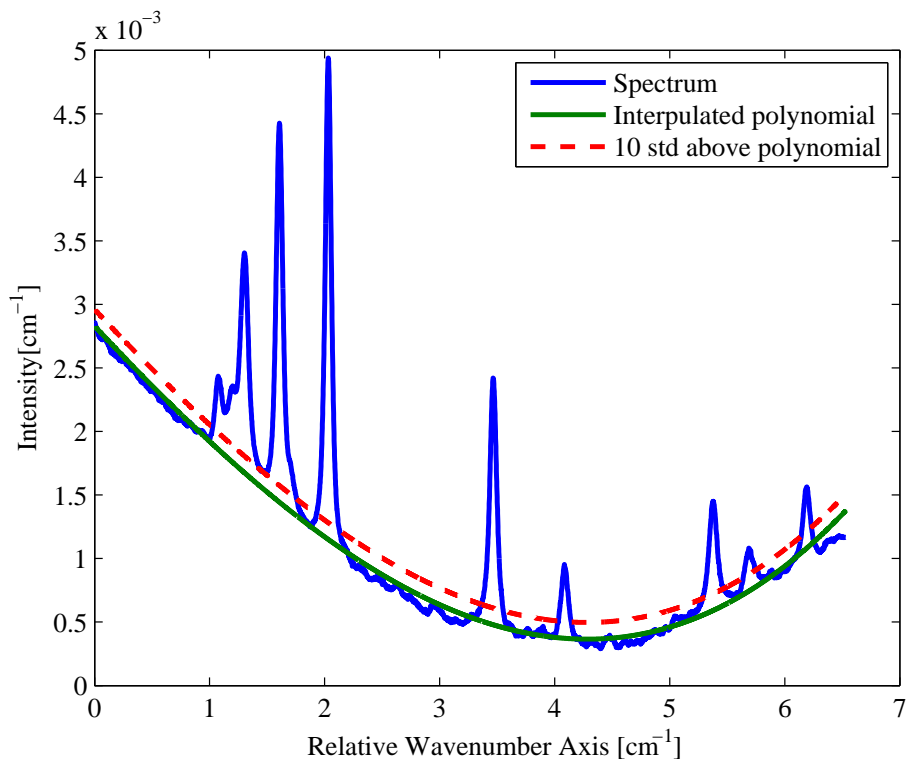
Figure 4.8: This figure depicts a third order polynomial fit to the minimums of a spectrum. The red dotted line shows the region which is ten standard deviations of the noise above the polynomial.

Once the polynomial curve was shifted by 10 standard deviations all of the points above the that curve were set to the value of the non-shifted polynomial (the green curve in the figure).

This process was then modified and repeated on the new curve with the features pulled down to the polynomial curve. A few modifications were made to this method, such as; 1) using all of the data points to fit the polynomial (instead of just local minimums), 2) using only 2 standard deviations instead of 10, and 3) using a much higher order polynomial, near 15. The higher order polynomial was used to better match what remained of the features, because after the initial low ordered polynomial the majority of the features remaining were from the baseline. This process was then

repeated without modifications until the case was reached such that fitting the data to the next polynomial found no new points above 2 standard deviations above that curve. This curve was then considered to be the baseline and was subtracted from the non baseline-corrected spectrum.

Figure 4.9 shows method 2 applied to a spectrum. In (a) the uncorrected spectrum is shown in blue with the calculated baseline in green. In (b) the baseline correction from method 2 was applied to the spectrum by subtracting the baseline from the uncorrected spectrum.

(a) No baseline correction   (b) Baseline correction applied
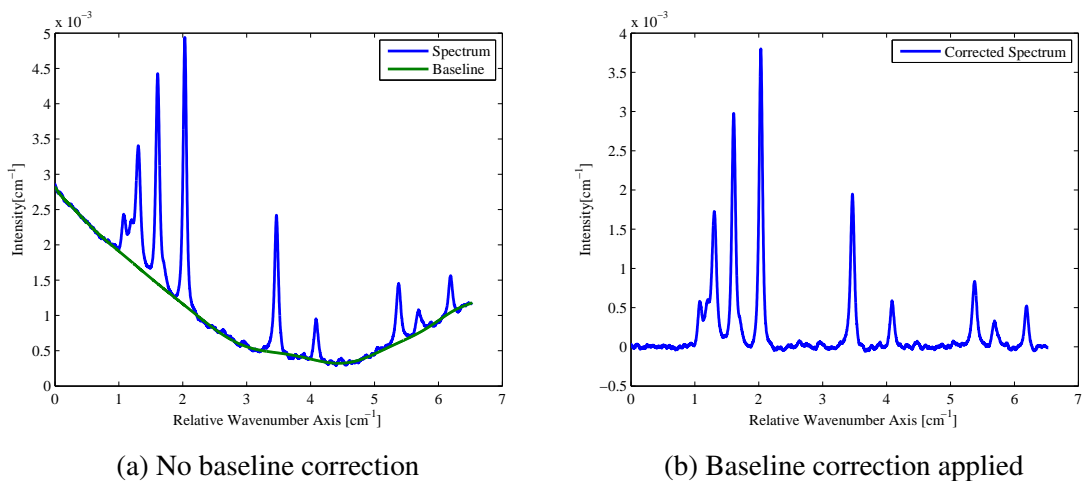
Figure 4.9: This figure illustrates the corrections made to a baseline using method 2.

This method, while it did not always produce as flat of a baseline as the first method, worked for a larger range of situations, and rarely had to be adjusted from one scan to next. This method was much more suitable for high pressures than method 1, however, it was not able to handle high pressures well enough to extract useful temperature measurements. This method was not exclusively used over the first method because for the cases when the slope of the baseline changed rapidly, this method had trouble because the polynomials would not fit to the features well.

4.9   Reducing the Noise

Reducing the noise improved the fit to the data, particularly when the data could not be averaged. Reducing the noise was done in a similar fashion as the smoothing was done for the baseline correction, however, the Gaussian used to reduce the noise was more narrow, to reduce the broadening effect on the spectral features from the convolution. A FWHM of 0.002 cm^{-1} was used because that was considerably more narrow than the spectral features encountered, and was on the order of the width of the noise in the data. Figure 4.10 shows a spectrum with and without the noise reduction applied, and the associated residual between the two.
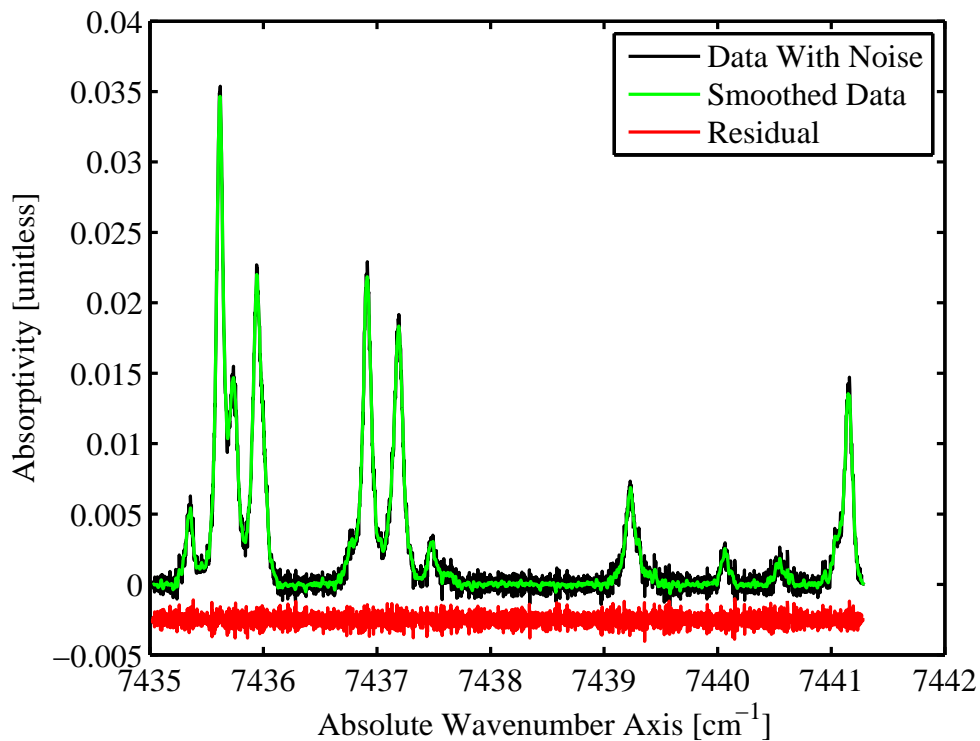
Figure 4.10: This figure compares the spectrum with and without smoothing. The residual in red is artificially shifted vertically by 0.0025 to allow for better visualization.

4.10   Program User Interface

A complex graphical user interface (GUI) was developed to interactively process the raw spectral data collected with the TDM-TDLAS system. Figure 4.11 shows the start up screen for the GUI. The red numbers correspond to the different sections of the GUI which will be discussed in detail below.
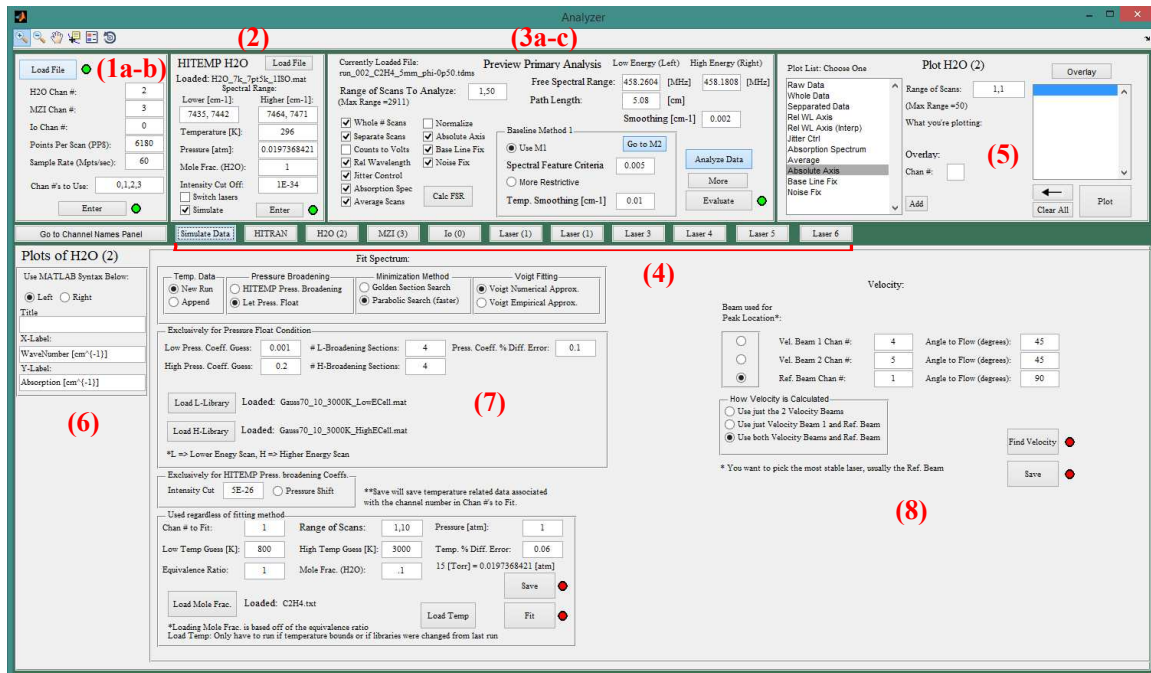

Figure 4.11: This figure shows the start up screen of the GUI created to analyze the raw data collected by the TDM-TDLAS spectrometer.

4.10.1   Load Window (1a-b).

Figure 4.12a shows a close up of the Load Window found at (1a-b) in Figure 4.11. The primary function of this window is to load raw spectral data which is saved by the LABVIEW code. The file format must be '.tdms' which is an acceptable format for LABVIEW. This is accomplished by first selecting the *Load File* button. This button prompts the user to select a file using the standard Windows file browser. When a file

is selected the red indicator light next to the *Load File* button turns green to inform the user that the path to their file has been successfully retrieved.

Underneath the *Load File* button in Figure 4.12a there are a 6 text boxes on the right which can be edited by the user. The first three ending in *Chan #:* are used to determine which channel (BNC port) on the Data Acquisitions board (DAQ) the specified laser signal will be recorded on. The number entered in the text box for *Points Per Scan* is the number of data points for an entire scan through both the low and high energy lasers. The *Sample Rate* is the rate in mega points per second. The last text box, *Chan #'s to Use:*, is used to specify all of the channels of data the user wishes to load, including both the interrogating laser channels and the three channels in the previous text boxes. The *Enter* button is used to load the specified channels from the file selected earlier.

Once the file is loaded the indicator light turns green and the Load Window automatically changes to the Channel Names Panel shown in Figure 4.12b. This screen allows the user to assign custom names to the channel numbers. These names are updated on the plotting tabs found in Figure 4.15. This is done to help keep track of each laser's use in the experiment. The toggle button at the bottom of both GUIs in Figure 4.12 is used to switch back and forth between the Load Window and the Channel Names Panel.
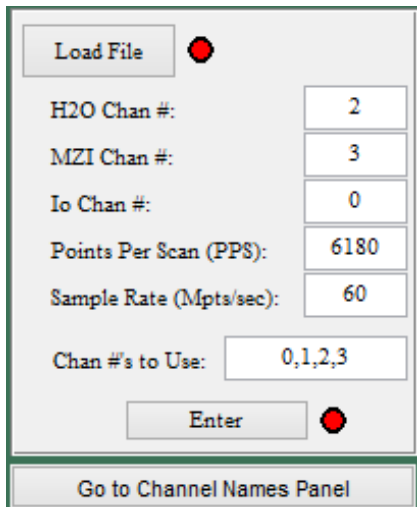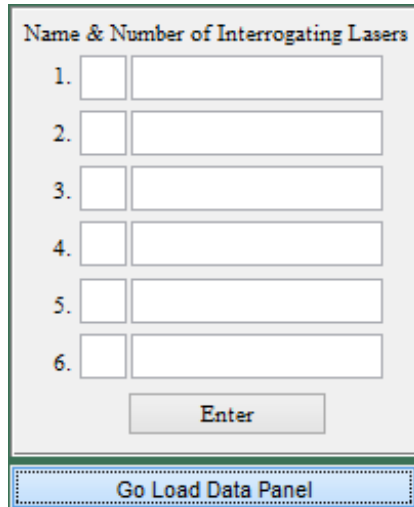
| (a) Load Window | (b) Channel Names Panel |

Figure 4.12: This figure shows the Load Window and Channel Names Panel. The Load Window is found at (1a-b) in Figure 4.11. The Channel Names Panel can be accessed by clicking on the *Go to Channel Names Panel* button.

4.10.2   Loading HITEMP (2).

Figure 4.13 shows the HITEMP panel which can be found at (2) in Figre 4.11. The primary purpose of HITEMP panel is to allow the user to load spectral data from the HITRAN/HITEMP databases. The file format currently supported is a MATLAB data file '.mat'. To increase the generality of the program '.txt' files will be supported in later versions. Upon startup of the GUI there is a default file path loaded. However if the user does not wish to use that data file, the *Load File* button can be selected, which will ask the user for a new data file.
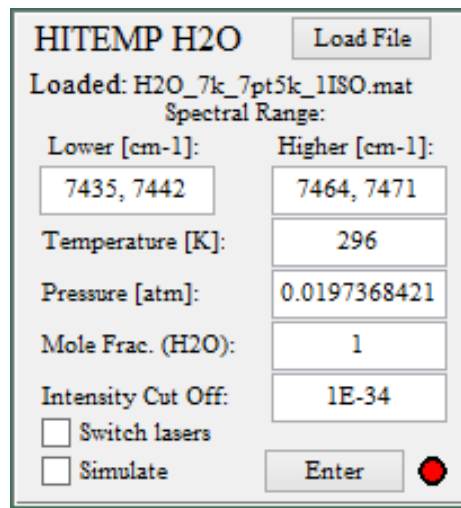
Figure 4.13: HITEMP load and simulate panel.

50

For the *Spectral Range* there are two editable text boxes. The first one on the left, *Lower [cm⁻¹]*, is used for the spectral range that the lower energy laser (or higher wavelength laser) scans. The right one, *Higher [cm⁻¹]* corresponds to the higher energy laser (lower wavelength). For simulation purposes, it is suggested the user chooses a range slightly larger than the range of the actual scan, usually an additional 0.5 to 1 wavenumbers on each side of the scan is sufficient. This prevents large broadenings from spectral lines just outside the scan range from being neglected during the simulation of the spectra. The temperature, pressure and mole fraction are used to simulate the spectral data from the water cell. To increase simulation speed there is the option to discard weak spectral lines for the temperature being studied. The value for the *Intensity Cut Off* text box specifies a minimum line intensity, any lines smaller than that number are discarded. This number refers to the intensity, S(T), calculated with Equation 3.5.

To simulate the data the *Simulate* check box must be checked, otherwise the non-broadened lines will be used in the calculation. This is a good approximation at room temperature, because the HITEMP lines are scaled for 296 K.

The *switch laser* check box allows the user to switch which spectral region of the HITEMP database is used to calculate the absolute axis on which the measured data is plotted. This check box should not be used under normal circumstances, and was primarily used for debugging purposes. The *Enter* button compiles the above requests and executes them.

4.10.3   *Primary Analysis (3a-c).*

As discussed in Section 4 there are a large number corrections that had to be made to the data before it could be fit with a simulated spectrum. The *Primary Analysis* panel, along with its sub-panels, handles this processing. These panels are located at (3a-c) in Figure 4.11, and can all be seen in Figure 4.14.

The *Primary Analysis* panel must be used for analyzing large data sets (more than 1,000 to 3,000 scans, depending on the user's available RAM). As a rule of thumb consider 2,000 scans for a 4 GB system, 5,000 scans for an 8 GB system, and 10,000 scans for a 16 GB RAM system, to be large data sets. This panel, shown in Figure 4.14a, evaluates the data faster and uses less RAM than the panel in Figure 4.14b. A limitation of this panel is that only the final version of the data, after it has been processed, can be viewed. The data for the various calculations is discarded during processing to save space on the computer's RAM.

To view data throughout its processing, the *Preview Primary Analysis* panel must be used. To access this preview mode, the *Preview Data* button must be selected in the *Primary Analysis* panel shown in Figure 4.14a. To return to the primary analysis mode, the *Analyze Data* button must be pressed in Figure 4.14b.

Data is processed the same in both the primary analysis mode and the preview mode, with the exception that the data throughout the processes are retained in the preview mode, therefore, both panels will be discussed together. In Figures 4.14a and 4.14b there are a large number of user options. The *Range of Scans To Analyze*, refers to the range of scans which the user wishes to process. The text *Max Range =* 2911 is used to inform the user of the maximum number of scans in a data set in order to prevent the user from trying to analyze too many scans. This maximum number of scans is only displayed here once data is loaded in the *Load Window*.

The check boxes in Figures 4.14a and 4.14b correspond to the data processing discussed in Section 4. The *Jitter Control* check box does not refer to laser jitter, but instead it refers to the jitter seen in the spectral scan range of the lasers as discussed in Section 4.5.

(a) Primary Analysis Panel

(b) Preview Primary Analysis Panel

(c) Addition Analysis Panel

Figure 4.14: This figure shows the panels used to process the data. Navigation between panels is achieved through the use of the *Preview Data, Analyze Data, More,* and *Less* buttons located at the bottom right of the figures.

Under the check boxes in Figures 4.14a and 4.14b, there is a button called, *Calc FSR*. This button allows the user to recalculate the FSR of both lasers used. When this button is pressed, the results are displayed in the two *Free Spectral Range* text boxes. The FSR should not need to be calculated more than once for the same set of laser diodes. There are, however, factors that can change the FSR for each of the diodes. Two primary factors which could change the FSR are; large changes in the spectral range the diodes are scanned across, and slight changes to the geometry of the MZI.

The path length traversed by the laser must be entered in the *Path Length* text box in centimeters. This number is used in Beer's law for the absorption coefficient calculations. The *Smoothing* text box is found directly under the *Path Length* text box. If the *Noise Fix* check box is checked, the *Smoothing* text box value determines the FWHM which is used to smooth the data with a Gaussian profile. The value of this parameter depends on the noise level of the data set. For the water cell, which contained a small etalon in the signal from the windows on the cell, a value of 0.01 cm^{-1} was found to work well for removing the etalons. For data without the etalon a FWHM of 0.002 cm^{-1} was found to work well.

The last set of processing options for Figures 4.14a and 4.14b are those found in the *Baseline Method #* panels. Figures 4.14a shows a different baseline panel than Figure 4.14b. The two baseline panels are used for controlling which baseline method is used and how it is applied. The baseline panels can be toggled back and forth using the *Go to M#* button. The number on the toggle button changes depending on which baseline method panel is active. The radial button *Use M#* determines which baseline method is used.

In the *Baseline Method 1* panel, active in Figure 4.14b, the *Spectral Feature Criteria* refers to the *C* value in Equation 4.4. The radial button *More Restrictive* refers to the 'or' in Equation 4.4. If the radial button is selected, the 'or' condition

is changed to an 'and' condition, making the selection of peaks more stringent. This option was sometimes necessary for data sets with low signal to noise ratios. The *Temp. Smoothing* text box refers to the FWHM of a Gaussian profile which is used in the code to temporarily smooth the data for the Method 1 baseline correction discussed in section 4.8.1.

The *Baseline Method 2* panel, active in Figure 4.14a, provides the control of the second baseline method discussed in 4.8.2. The *Order A* text box is the order of the polynomial used to increase the conversion rate of the baseline Method 2. The value of *Order B* is used for the iterative part of Method 2. *Order B* should usually be larger than *Order A*.

In Figure 4.14c the *Additional Analysis* panel is a sub-panel of the *Preview Primary Analysis* panel. It can be accessed by selecting the *More* button in Figure 4.14b. If the data is not processed in the *Preview Primary Analysis* panel before the *Evaluate* button is pressed in the *Additional Analysis* panel, then the data from both panels is calculated, otherwise only the additional data is processed in the *Additional Analysis*. The options in this panel are purely for viewing some of the different processes applied to the water cell and MZI. These options do no need to be selected to process the data.

4.10.4   Plot Buttons (4).

The plotting buttons can be found at (4) in Figure 4.11. These buttons are shown in Figure 4.15. All of these buttons with the exception of the *Simulate* button are used for plotting and viewing data. All of the buttons are used to change what is displayed directly underneath them and, with the exception of the *Simulate* button, create plots similar to those seen in Figure 4.17.
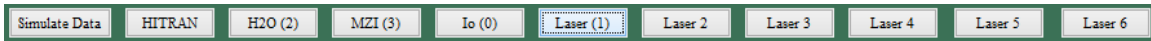
Figure 4.15: The buttons shown in this figure control what is displayed directly underneath them in Figure 4.11. All of them except the *Simulate Data* button are used for plotting purposes.

In Figure 4.15 the *Laser 1* button is shown as being selected. Selecting this button would perform the following tasks. First the display in the panel below it in Figure 4.11 is changed to display two figures which correspond to the Laser 1 channel. The second task the button performs is to update the list of plotting options shown in Figure 4.16. The *Simulate Data* button returns the panel back to the original startup configuration.

4.10.5   *Plotting Panel (5).*

The *Plot* panel seen in Figure 4.16 and at (5) in Figure 4.11 lets the user select what data to view. The plot button that is selected determines which laser data is shown. The options displayed in the *Plot List* list box are controlled by which plot button is selected and by

Figure 4.16: This is the *Plotting* panel used to plot the data which was processed

the corrections applied to the data as determined by the check boxes in the *Analysis* panels. The *Primary Analysis* panel does not save the data during the processing. When this panel is used the only options in the *Plot List* will be the raw data and the fully processed data.
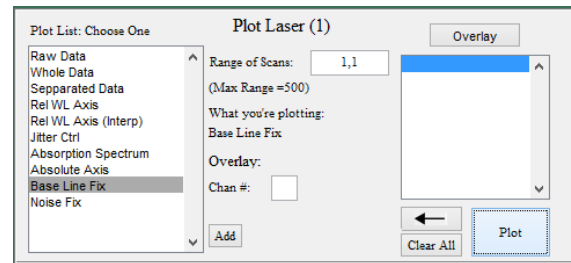
The *Range of scans:* text box selects the number of scans the user wants to plot at once. If the data was averaged, this value is ignored because there would only be one scan worth of data for a given channel.

The left arrow button de-selects the currently selected item to be plotted. The *Clear All* button clears all visible plots. This can also be accomplished by selecting the *Plot* button when there is nothing selected to plot. Additionally, the *Plot* button plots the currently selected item displayed under the *What you're plotting* text in the plots shown in Figure 4.17. The *Overlay* button is currently not used.

4.10.6   Figures (6).

Figure 4.17 shows region to the right of (6) in Figure 4.11 once a plotting button is selected. The features in the top left of the figure are not fully integrated into the code, so the user can not define axis labels. However, the arrows shown in the upper right hand corners above the plots in the figure allow the user to pull the figure out of the program into a normal MATLAB figure, with all of the options for editing figures that are normally provided by MATLAB.
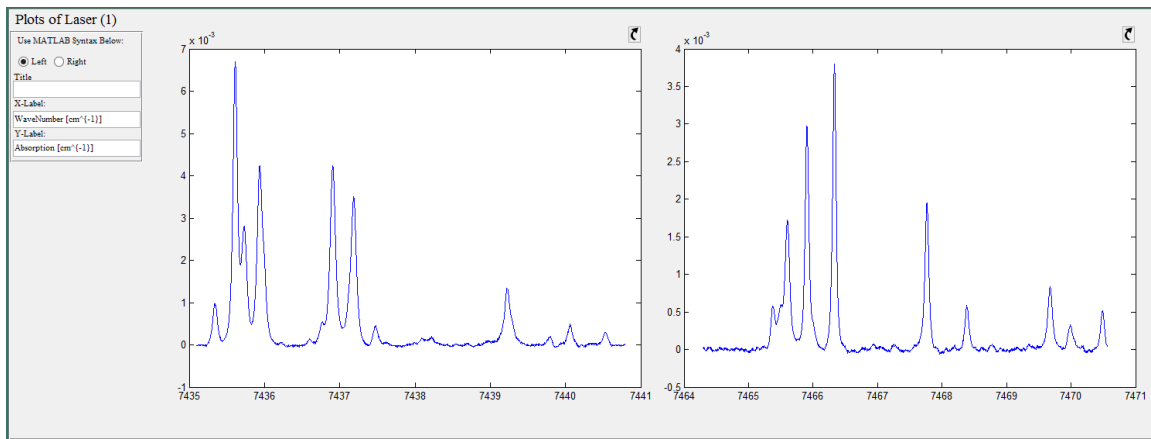

Figure 4.17: This figure shows the region in the GUI where the user can plot and visualize data.

4.10.7   Simulation (7).

The region in the GUI where the parameters can be edited for simulating the spectra to extract temperatures and water concentration is found near (7) in Figures

57

4.11 and in 4.18. There are a multitude of controls which determine how the spectra are simulated and fit to the data. In the top left of Figure 4.18 in the *Temp. Data* panel there are two options. These options dictate what happens to the data from previous runs. The *New Run* option replaces the old data with the current values. The *Append* option preserves the old data points along with the new ones. This allows the user to view and save the results from multiple experiments.

Figure 4.18: This figure shows the options for fitting the simulated spectrum to the measured data.

The *Pressure Broadening* panel provides two options. The first is *HITRAN Press. Broadening* which, if selected, will simulate the spectra using HITRAN/HITEMP pressure broadening coefficients. This method is considerably faster than the other option, *Let Press. Float*, which lets the pressure broadening float to the best value, however, the HITRAN broadening will be incorrect for high temperatures or pressures.

The *Minimization Methods* panel provides the user with two different methods to minimize the difference between the simulated spectrum and the measured spectrum. Both are published minimization methods and can be found in a variety of sources including Sauer [13]. The *Golden Section Search* method is more robust, and more likely to converge to a value, however, the parabolic interpolation search (*Parabolic Search*) is faster, yet more likely to fail. Thankfully, the latter is usually not a problem for the minimizations needed for this research.

The next panel in Figure 4.18 is the *Voigt Fitting* panel. Here the user can choose a method to simulate the spectrum; either the empirical method, described by Whiting [19], or the numerical method developed in this thesis.

Spectral lines can be shifted with pressure. This shift is applied when the radio button *Pressure Shift* is selected. However, it was found that applying the shift tended to reduce the agreement between the simulated data and the measured data.

The majority of the remaining simulation options are fairly straightforward, however, a few of them warrant explanations. The value for the *Mole Frac. (H_2O)* option can be determined from NASA's Chemical Equilibrium with Applications (CEA) code or some other similar code for calculating adiabatic concentrations. The *Load Mole Frac.* button can be used to load a text file which contains various equivalence ratios and their respective mole fractions for a particular fuel. The default fuel is C_2H_4. Entering an equivalence value into the *Equivalence Ratio* text box will update the *Mole Frac. (H_2O)* with the correct mole fraction for that fuel and equivalence ratio.

In the *Exclusively for Pressure Float Condition* panel and the *Used regardless of fitting method* panel there are two text boxes dealing with error in calculating the temperature and pressure broadening coefficients. These errors are a measure of how close the simulated spectrum comes to the best possible value the simulation could produce.

In Figure 4.18, in the *Exclusively for Pressure Float Condition*, there are two buttons, *Load L-Library* and *Load H-Library*. These buttons are used to load libraries of precomputed spectral lines over a range of temperatures. The spectral lines in the libraries are only Gaussian broadened. The libraries are used to reduce the number of calculations that are required when letting the pressure float.

The *# L-Broadening Sections* and *# H-Broadening Sections* text boxes are used to set the number of pressure broadening coefficients used to fit the lower and higher energy spectra, as discussed in section 3.2.5.2.

4.10.8   Velocity (8).

The final set of controls the GUI offers are for determining the velocity of the medium. This code determines the velocity by calculating the Doppler shift of the spectral profiles. To do this at least two laser beams are required at different angles to the flow.

The first option is a set of radio buttons in the *Beam used for Peak Location* panel. This lets the user pick which of the laser beams will be used to find the location of a peak for velocity measurements. The best choice is the interrogating laser with the most stable signal (the one which suffers the least from beam steering throughout the experiment). The channel numbers and the angles for the beams can be found to the right of the radio buttons.

In the *How Velocity is Calculated* panel there are three choices. The first choice is to use two beams which are angled to the flow. In this method the non-Doppler

shifted spectral line is assumed to be between the two shifted peaks. The second choice uses only one velocity beam and the reference beam. The reference beam is angled 90 degrees to the flow, so the spectral features measured by this beam are not Doppler shifted. The last choice uses two velocity beams and the reference beam to calculate the velocity. The calculations made with the second choice are less accurate than the other two choices because this choice only measures the Doppler shift once, while the other methods measure it twice. The last choice is the most accurate because it uses all three measurements; the reference beam and the Doppler shift in both directions.

The *Find Velocity* button takes the user input and calculates the velocity with the measured spectra provided. The results from the velocity calculations can be saved in a text file using the *Save* button.

Figure 4.19: This figure shows the options the user has available for determining the velocity of the interrogated medium.

61

V.   Hencken Burner

5.1   Theory

The Hencken burner was used because it provided a flat, steady, near adiabatic flame for which mass flow rates and equivalence ratios could be controlled. The Hencken burner that was used had a rectangular array (5.08 x 2.54 cm) of fuel and oxidizer tubes surrounded by a rectangular array of tubes for inert gas which prevented the fuel from mixing with ambient air. The oxidizer tubes were slightly recessed below the fuel tubes to help lift the flame off of the burner surface to reduce heat transfer from the flame to the burner surface.

Adiabatic flames have zero heat transfer between the flame and its environment. This is an ideal condition and never realizable. However, the adiabatic temperature of a flame can be used to determine a temperature limit for a real flame. For some conditions, such as those that can be obtained using a Hencken burner, the real flame can get very close to the ideal adiabatic flame. For these conditions adiabatic temperatures provide good predictions and comparisons to the measured flame temperatures.

Adiabatic flame temperatures were used in this experiment to compare the measured flame temperatures of ethylene (C_2H_4) and methane (CH_4), from a Hencken burner, at various equivalence ratios and heights above the burner surface. Adiabatic temperatures were calculated using NASA's CEA code [5].

Different equations are used for calculating adiabatic temperatures for different scenarios. The 'HP' (enthalpy and pressure) problem was solved using CEA code for the Hencken burner adiabatic temperatures. The 'HP' problem is used for calculating constant pressure combustion parameters, one of which is the adiabatic flame temperature [5]. For the 'HP' problem, the equation that needed to be solved could be

written as [17],

$$H_{react}(T_0, P) = H_{prod}(T_{ad}, P), \qquad (5.1)$$

where H_{react} and H_{prod} are the total enthalpy [joules] of the reactants and products respectively, T_0 is the initial temperature of the reactants, P is pressure, which is assumed to be constant throughout the reaction, and T_{ab} is the adiabatic temperature of the combustion. This equation states that energy is conserved throughout and within the combustion process. This not only means that energy was not created or destroyed, it also means that there was no energy lost or gained from the system into the surrounding environment. Each side of Equation 5.1 can be expressed as a summation of the enthalpies of all of the reactants and products yielding [17],

$$H_{react} = \sum_{i=1}^{\#react.} N_i \bar{h}_{f,i}, \qquad (5.2)$$

and

$$H_{prod} = \sum_{i=1}^{\#prod.} N_i (\bar{h}_{f,i} + \bar{c}_{p,i}(T_{ad} - T_0)), \qquad (5.3)$$

where N_i is the number of moles of the ith species, $\bar{h}_{f,i}$ is the enthalpy of formation in joules per mole of the ith species and $\bar{c}_{p,i}$ is the constant pressure specific heat in joules Kelvin per mole of the ith species. The additional term, $N_i(\bar{c}_{p,i}(T_{ad} - T_0))$, in Equation 5.3 accounts for the energy released from the chemical bonds of the reactants during combustion.

The variables in Equation 5.2 are generally known for a given problem (the reactants are usually known in experiments). The difficulty in calculating the adiabatic temperature arises in determining what the products are and their quantities. For the constant pressure problem the determination of the products and their quantities is accomplished by the minimization of the Gibbs function. The Gibbs function is defined as,

$$G \equiv H - TS, \qquad (5.4)$$

where the only new variable S is the entropy of the system. A paper by NASA [5], discussing the CEA program, goes into detail on assumptions used in the calculation of the adiabatic temperature, as well as how the Gibbs function is minimized.

5.2   Experimental Setup

The Hencken burner was studied over a range of equivalence ratios at different heights above the burner surface. C_2H_4 and CH_4 were used as the fuels because of the high water content in the products of their combustion with air. Spectral data was taken with the TDLAS system discussed earlier. These measurements were fit with simulated spectra using HITEMP data to extract the path-averaged flame temperature and water concentration.

Figure 5.1 shows the setup for the Hencken burner experiment with a visible laser beam overlaid on the image. The two white ceramic pipes shown in the figure allowed the beam path before and after the flame to be purged with nitrogen to prevent room temperature H_2O absorption features from being detected. The laser beam was collimated across the flame and then was focused on the InGaAs detector (shown on the right in Figure 5.1). To align the laser, the (x,y,z) spatial directions were adjusted for both the laser pitch and catch (laser collimator on the left, and detector on the right, respectively) until the maximum response from the detector was observed.
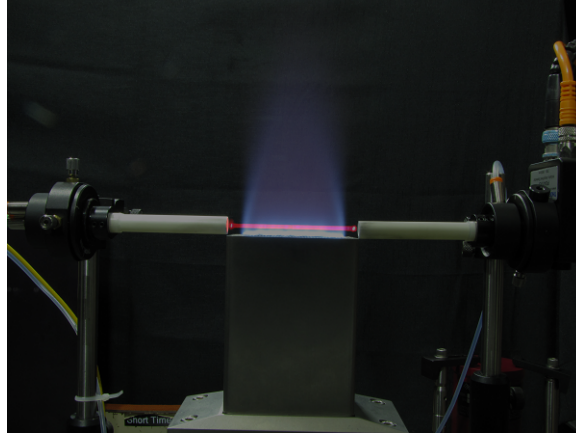
Figure 5.1: This is an image of the experimental setup with the Hencken burner. An image of a laser beam was superimposed across the flame to show the path of the near IR laser beam used to collect data.

5.3 Results & Analysis

5.3.1 Ethylene-Air, Temperature.

A large range of measurements were taken across the Hencken flame for three different heights above the burner; 5 mm, 10 mm , and 15 mm. At each of these heights, measurements were taken from an equivalence ratio of 0.5 to 1.5 at 0.1 increments for the C_2H_4 flame. Figure 5.2 shows the temperature calculated from the spectral data collected 5 mm above the flame for each of the equivalence ratios.

Figure 5.2: The average Hencken burner temperature versus equivalence ratio of C_2H_4 combusted in air at 5 mm above the burner surface is sh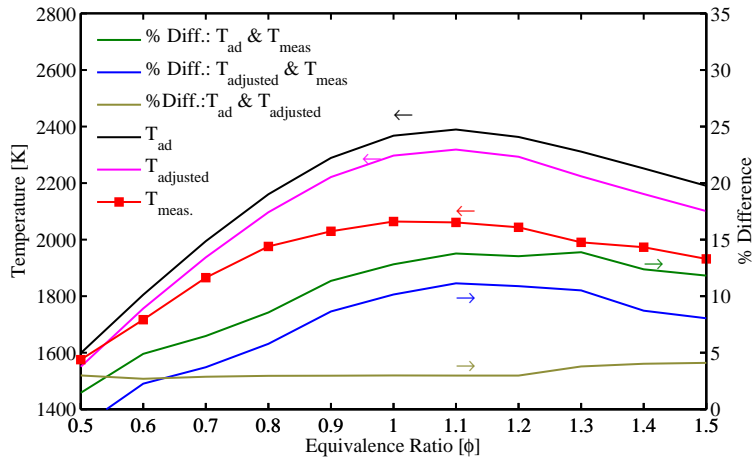own in red. The reactants were at standard temperature and pressure. The black line is the adiabatic flame temperature calculated with NASA's Chemical Equilibrium with Applications (CEA) code. The magenta curve shows the adiabatic curve adjusted for edge effects. The percent differences between the curves are shown as well. The arrows above the curves point to the applicable y-axis for the curves.

The temperatures were calculated by fitting averaged spectra taken with the spectroscopic system with simulated spectra generated using the HITEMP database and letting the pressure broadening float. For low equivalence ratios the data agreed extremely well with the adiabatic temperatures ($\approx 2\%$ difference). However the agreement worsened as the temperature increased with a maximum percent difference near 13%. Edge effects, heat loss, and non-uniformities along the beam path were believed to have been the contributing factors to this growth in percent difference with temperature.

Edge effects are caused by the gradient in temperature and mole fractions near the edges of the flame. To gain a qualitative understanding of how much the temperature measurements were effected by the edge effects, OH planar laser-induced fluorescence (PLIF) was used to determine the flame profiles at the various equivalence ratios. Figure 5.3 shows the flame profile 5 mm above the flame (corrected for laser

66

absorption) for two different equivalence ratios. Similar curves can be found in a paper by Meyer [8] for the mole fraction on a C_2H_4-air Hencken burner flame. The red curves were extracted from the black curves for each of the equivalence ratios and used to find a mole fraction weighted average of the adiabatic temperature. The adjusted adiabatic temperature is plotted in Figure 5.2 as the magenta curve. This shows that changes in the flame profile, and thus the edge effect, can have significant effects on the temperature.

The second cause for the large differences between the adiabatic and measured temperatures at high temperatures was heat loss to the burner surface and the surrounding air. There will always be some heat loss to the environment, and thus adiabatic temperatures can never be reached. As temperature increases, so does the temperature gradient between the flame and the environment, so heat transfer rate (or heat loss) increases. While the Hencken burner was designed to reduce

Figure 5.3: This figure shows OH PLIF profiles at 5 mm above the Hencken burner at equivalence ratios of 0.5 and 1.5. The curves are corrected for laser absorption and normalized to one. The red curves are the extracted profiles from the black curves used to adjust the adiabatic temperature for edge effects.

heat loss, the higher temperatures will still cause the flame to diverge more from the adiabatic ideal. The shapes of the percent difference curves reflect this. Once the temperature dropped after a $\phi \approx 1$ so did the percent difference between the adiabatic curve and the measured curve, shown in Figure 5.2.

As mentioned before, the temperature measurements were taken at three different heights above the burner surface. Figure 5.4 displays the average measured
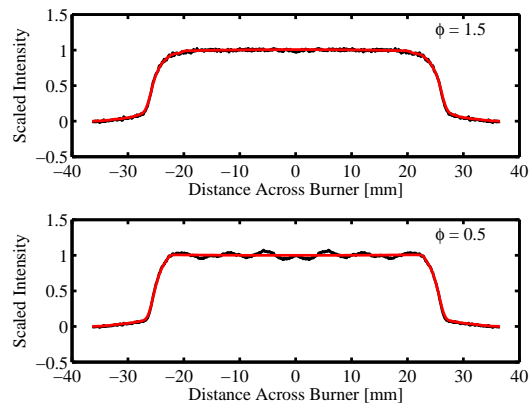
temperatures at the three different heights. Additionally, the temperature results 5 mm above the burner surface were compared to those calculated with a preexisting program (2nd method in Figure 5.4). The percent difference between the temperatures found using the second method and the temperatures calculated using the method developed in this research reveals a good agreement between the two methods with the largest percent difference near 1.5%.
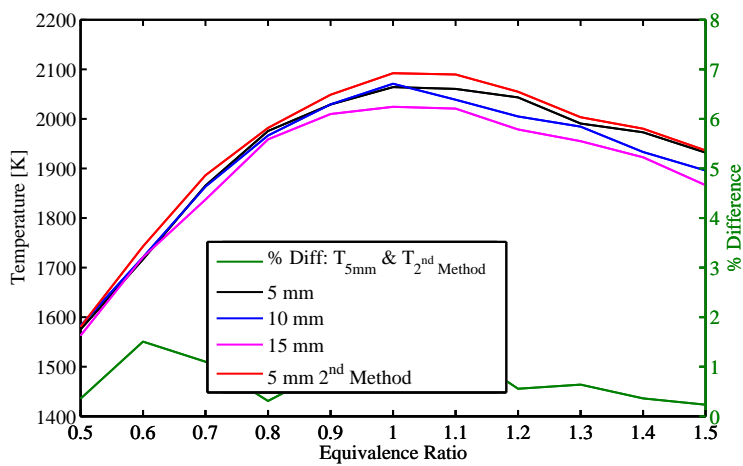
Figure 5.4: This figure shows the average measured temperatures of the C_2H_4 flame for three different heights above the burner surface.

5.3.2   *Ethylene-Air, H_2O Concentration.*

The water concentrations of the combustion products of C_2H_4 and air were found using the method discussed in section 3.2.5.2. The water concentration, like the temperature, was altered by the edge effects. Figure 5.5 displays the results for the measurements at three heights above the burner surface. The results, as expected, were lower than the adiabatic concentrations found using the CEA code, however, they do follow the same trend. The CEA adjusted water concentration (Figure 5.5) was calculated in the same manner as the adjusted adiabatic temperature, using the PLIF profiles.
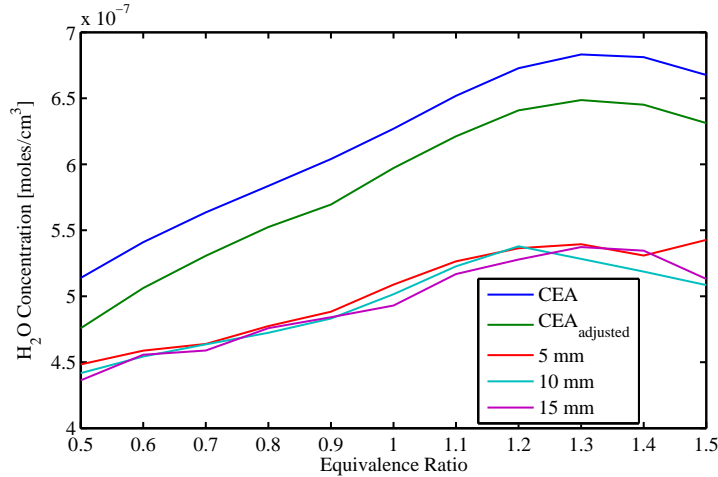
Figure 5.5: This figure shows the average measured water concentrations for the C_2H_4 flame at three different heights above the burner surface compared to the CEA calculated concentration, and the CEA concentration adjusted for edge effects.

The measurements produced by the spectroscopic techniques used in this research were path averaged measurements. There was no spacial resolution. The detector observed the final laser signal after it traversed the whole test medium. Any non-uniformities, such as there being small flamelets as opposed to a uniform solid flame, would change the signal. In the regions between flamelets the temperature would be cooler and the water concentration would be lower than it would be had there been a solid uniform flame. Because the measurements taken were path averaged measurements the hotter and cooler regions were averaged together ultimately resulting in a lower observed temperature than in the regions were there was a solid flame. This applied to concentration measurements as well. The edge effects discussed earlier are a specific case of non-uniformities along the beam path. Results for the methane flame can be found in Appendix B.
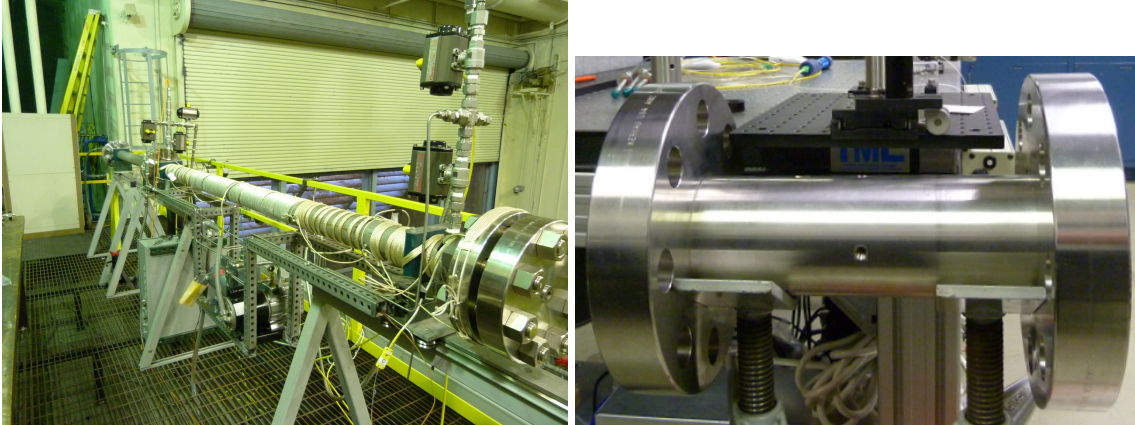
VI.   Detonation Tube

6.1   Theory

Detonation tubes provide an environment where high pressure, temperature, and velocity can be studied. These conditions are provided by a shock wave which propagates at the front of a detonation. To understand a detonation tube, it is important to understand the basics of a detonation.

"A detonation is a shock wave sustained by the energy released by combustion" as stated by Turns [17], and the combustion is initiated by the compression caused by the shock wave of the reactants. A detonation can be initiated by either a shock wave or by tripping the boundary layer of a propagating deflagration such that it becomes turbulent. A detonation is a complex three dimensional flow which is strongly dependent on the geometry of the confining tube [17] if there is one. However, detonations can be much more easily conceptualized using the Zeldovich, von Neumann, and Döring (ZND) model. This model illustrates a detonation as an idealized one dimensional flow of a shock wave followed by a combustion zone. While this is a simplified version of what really happens, this model provides a means to approximate pressure, temperature, and velocity directly following the shock and at the end of the combustion region. The conditions directly after the shock can be found by using the ideal shock equations which are developed by Liepmann [6]. The conditions after the combustion region can be calculated using equations developed by Turns [17].

6.2   Experimental Setup

The detonation tube is shown in Figure 6.1a. On the right side of the figure, two flanges can be seen bolted together. During the experiment the test section shown in Figure 6.1b was inserted between these two flanges. This test section had two optical

ports which were perpendicular to the test section. These ports had fibers adhesively held in place. The spectroscopic system used in the Hencken burner experiment was employed here as well.

(a) Detonation tube.

(b) Test section without fibers attached.

Figure 6.1: This figure depicts the detonation tube, (a), used in the experiments, and the test section, (b).

Measurements were taken at different equivalence ratios as well as different starting pressures of the detonation mixture, hydrogen-air. To make sure the mixture within the detonation tube was known, the detonation tube was evacuated prior to an experimental run. The tube was then flushed with air, and then pressure was pumped back down. This was to ensure the products from previous experiments were removed. The the tube was filled with air (the oxidizer) to a desired pressure below 1 atm. The tube was brought to atmospheric pressure by filling it the rest of the way with hydrogen (the fuel). For experiments with initial pressures above atmospheric pressure the detonation tube was pumped first with the oxidizer (air) and then with the fuel (H_2).

Once the detonation tube was filled with the H_2-air mixture, mixing pumps were run for 2 to 5 minutes to ensure the fuel was mixed before ignition. Once this was

71

complete the detonation tube was completely sealed off from the pumps. At the far end of the detonation tube, the opposite end from the test section, a spark plug was used to ignite the fuel. Within the detonation tube there was a spiral. This spiral was used to trip the flow, causing turbulence which increased the rate at which a combustion within a tube transitioned into a detonation.

6.3 Results & Analysis

Figure 6.2 shows the first 15.5 ms of spectral data recorded during one of the experiments. The scans were not separated in Figure 6.2, thus the bottom points are where bother lasers were off. This means that the changes in the bottom part of the curve were purely radiative emission from the test section. The prominent features near 8 ms were caused by the radiation produced by the combustion region just behind the detonation wave. The first large peak was caused by the initial detonation as it passed through the laser beams. The second larger peak was believed to be caused by the reflected shock off of the end of the detonation tube directly after the test section. The smaller rises seen near 11 and 13 ms were believed to be small reflections from the ignition end of the detonation tube. In a sense, the detonation bounced back and forth between the ends of the tube, however, it may have only remained a detonation wave after the initial reflection. Once the fuel was completely combusted, it would exist as a shock wave, continuously losing energy until equilibrium was reached.
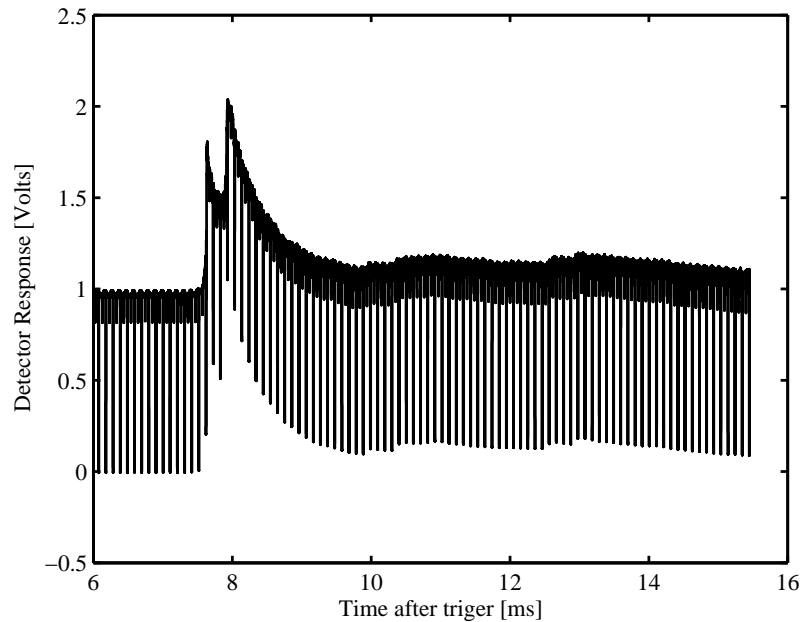
Figure 6.2: This figure shows the first 15.5 ms of intensity data recorded for one of the detonation tube experiments. The first large feature was created by the combustion region behind the initial detonation wave. The second large feature was from the reflected shock off of the end of the detonation tube.

Figure 6.3 shows the spectra for both laser scans approximately 9 ms into the experiment. These spectra were taken immediately after the reflected detonation wave passed the interrogating region, near 8.5 ms in Figure 6.2. The highest pressure conditions would most likely occur closer to the detonation. However, while these spectra may not have occurred at the highest pressure region, they are very broadened, and thus temperature calculations become challenging. Further research and code development needs to be accomplished before the temperature values can be extracted from these highly pressure-broadened spectra.
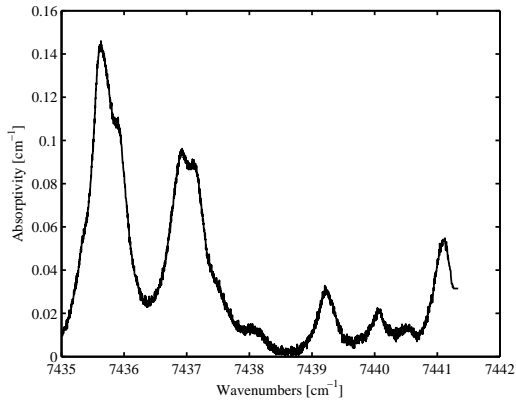
(a) Lower energy laser scan.
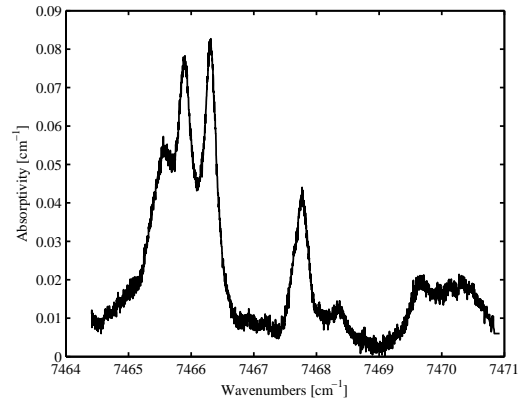
(b) Higher energy laser scan.

Figure 6.3: This figure shows spectra from both the lower and higher energy laser scans. This data was taken approximately 9 ms into the run
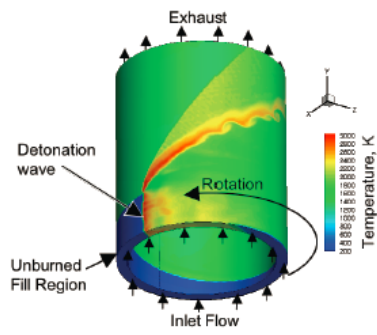
VII.   Rotating Detonation Engine

7.1   Theory

RDE's are mechanically very simple engines with no moving parts. They utilize the higher efficiency of detonations to convert chemical energy into mechanical energy as opposed to non-detonation combustions (deflagrations) which conventional combustion engines use today. The mechanical components of the RDE are physically simple, however the gas dynamics are very complicated and much concerning the operation parameters of an RDE are unknown and are the subject of considerable research.

In an RDE the fuel is initially ignited using a pre-detonation mixture. After the initial ignition the detonations are self-sustaining with the continued addition of fuel and oxidizer. A detonation wave propagates around an annulus created by the inner and outer body shown in the Figure 7.1b. The inner and outer bodies are two cylindrical structures, one inside of the other.

To sustain the detonation a fuel-oxidizer mixture (hydrogen-air) has to be continuously introduced into the system near the bottom of the detonation channel (annulus) shown in Figures 7.1b and 7.1a. This provides the detonation wave with fresh H_2-air every time it returns to a particular point in the channel [11]. This process is depicted in Figure 7.1a from a paper by Schwer [15]. Exhaust flow out of the RDE is produced by the expansion of the detonation waves.

(a) The cyclic process of an RDE as shown by Schwer [15].
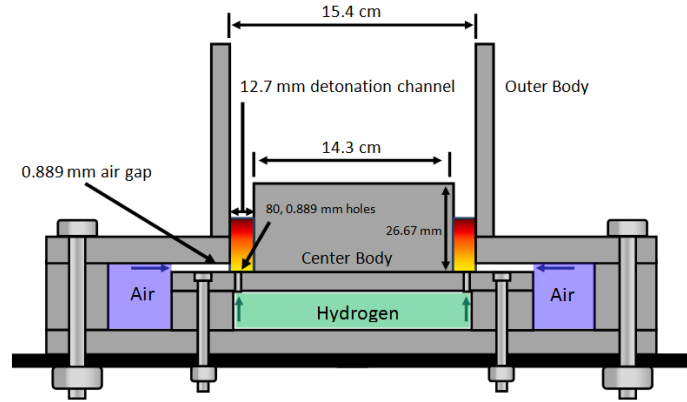
(b) RDE cross-section with some dimensions labeled. [10].

Figure 7.1: These figures together help describe how a rotating detonation engine works. Figure (a) shows a simulated view of how the detonation wave propagates within in the detonation chamber as created by Schwer [15] (with permission from Elsevier). Figure (b) shows the cross-sectional view of the RDE. This figure was modified from a figure by Naples [10].

7.2 Experimental Setup

The spectroscopic system and the RDE were placed in separate rooms to protect the system from the harsh acoustic environment produced by the RDE. Optical fibers were used to carry the laser beams from the spectroscopic system to the RDE. The detectors were kept in a box near the RDE system. The signal from the detectors was transmitted through BNC coaxial cables back to the spectroscopic system and recorded by the computer.

Six laser beams were used. The first was used for the H_2O cell, the second was for the MZI, the third was used for the reference intensity I_o, and the other three were used to interrogate the RDE exhaust. The three interrogating lasers were connected to the test section shown in Figure 7.2.

Figure 7.2 shows a front and side view of the RDE setup. The front view, Figure 7.2a, shows the laser fibers attached to the optical ports on the test section. One of

the three interrogating lasers was used to measure the temperature of the exhaust gas. This laser was oriented perpendicular to the flow and was pitched and caught at 1 and 2 in Figure 7.2a respectively. The other two interrogating laser beams were used to take data for velocimetry measurements. One of these velocimetry lasers was pitched downstream (with the flow) at a 45º angle. The other was pitched upstream (against the flow) at a 45º angle. This allowed for both the blue and red Doppler shift effect on the spectral features to be observed. From the Doppler shifts the velocity of the flow was determined. For the velocimetry lasers dual ended fibers were used so both beams were able to share the same optical ports. In the dual fiber one of the fibers pitched a laser, and the other fiber caught a laser. The two optical ports for the velocimetry beams are shown in Figure 7.2a at 3 and 4. Each optical port, at 1, 2, 3, and 4 in the figure was purged with nitrogen to remove ambient temperature water vapor from the laser beam paths. One of the white purge lines can be seen clearly at 5.
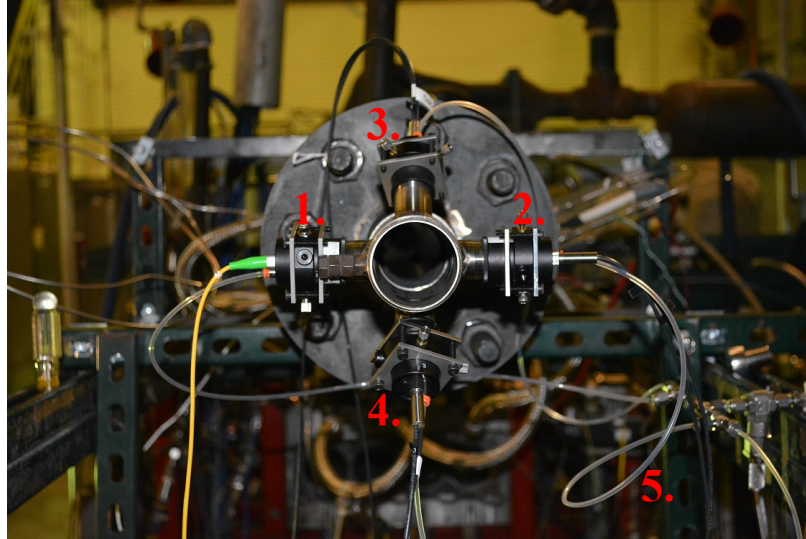
(a) Front View
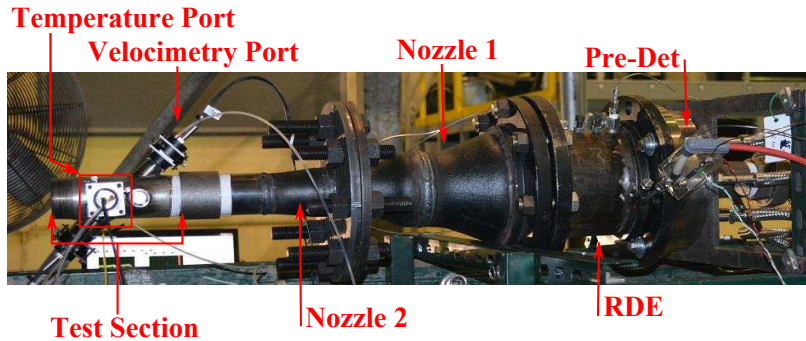
(b) Side View

Figure 7.2: This figure depicts the front and side view of the RDE with the test section attached. In the front view (a) the pitch and catch for the temperature laser can be seen at 1 and 2 respectively. The pitch and catch for both velocimetry beams are located at 3 and 4. All four optical ports were purged with nitrogen with the white plastic purge line best seen at 5. The side view (b) shows the RDE. The nozzles are labeled, as well as other important parts of the RDE.

The side view of the RDE system, Figure 7.2b, shows the actual RDE, the pre-detonation device, both nozzles and the test section with the velocimetry and temperature ports. The first nozzle drops the flow diameter from 15.4 cm to 6.35 cm. The second nozzle drops the flow diameter from 6.35 cm to 5.08 cm. These nozzles allowed the test section, which had a diameter of 5.08 cm, to be connected to the RDE.

7.3   Results & Analysis

To initiate the detonation, a pre-detonation device was used. This device filled the detonation chamber with a hydrogen-oxygen mixture before the RDE was ignited. The operating fuel (as opposed to the fuel used to initiate the detonation) was a hydrogen-air mixture. The mass flow rate of the air was kept at 30 lbs/min for all of the experiments and the equivalence ratios were changed by adjusting the fuel flow rate.

Velocity, temperature, and concentration were calculated from the measurements taken down stream of the nozzle at the test section shown in Figure 7.2. Because the conditions in the RDE change with time, the velocity, temperature, and concentration were calculated for each scan of the spectroscopic system for the first 200 ms of the experiment. The regions where the RDE reached a steady state were averaged together to produce average values for each of the calculations.

7.3.1   Velocity.

Figure 7.3 shows the time series of the exhaust velocity for an equivalence ratio of 1.419. Outliers more than three standard deviations were excluded from this plot. These outliers could be ignored because they resulted from the decoupling of one or both velocimetry interrogating lasers. There are a number of events which could cause the laser to decouple. The first is beam steering. Beam steering can be caused by shock waves, turbulence in the flow, and by large temperature gradients. The beam can also be decoupled by changes in the temperature of the test section's structural components. This causes the test section to change size slightly which can change the angle at which the lasers are aligned. The lasers can also be decoupled by the vibrations caused by the detonations in the RDE, as well as debris, such as soot. Velocity curves for the other equivalence ratios studied in this experiment are shown in Appendix A. Some of these curves show a faster initial velocity, which was caused by the initial detonation of the

RDE. However, in others (such as the velocity time series shown in Figure 7.3) the velocity was truncated. This truncation occurred due to the decoupling of one or both velocimetry beams. The velocity data in Figure 7.3, as well as those in Appendix A, show that the RDE reached a stable operating condition after the initial detonation. The time to reach this steady state varied from experiment to experiment, however, it always occurred before 50 ms and usually closer to 15 ms.
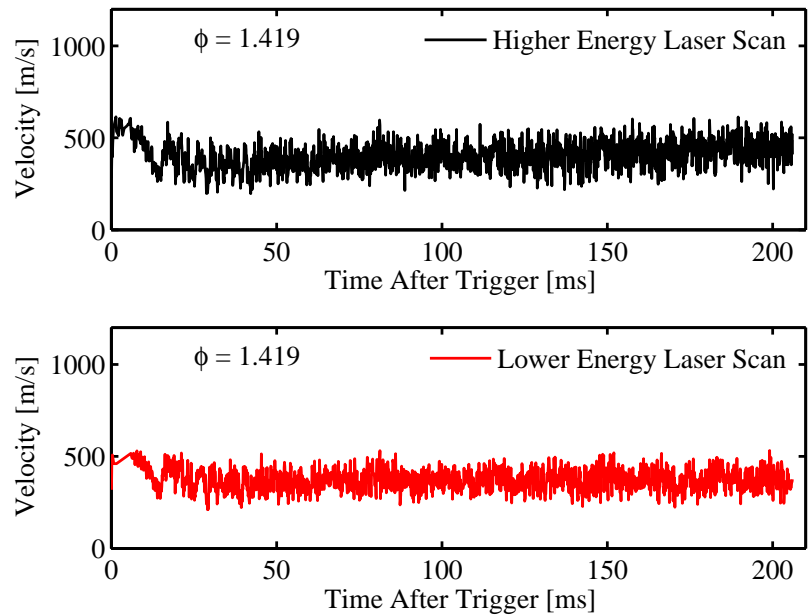
Figure 7.3: This figure shows the velocity time series for both sets of wavenumbers scanned (higher and lower energies).

Figure 7.4 shows the dependence of the exhaust velocity of the RDE on the equivalence ratio. The black data points in Figure 7.4 are the averaged steady state velocities obtained from the higher energy laser and the red points are from the lower energy laser. The black and red curves in the figure are the first order fits to their correspondingly colored data sets. As can be seen by the R^2 value, as well as the scattering of the data points, the velocity was not dependent on equivalence ratio. This occurred because the velocimetry measurements were taken down stream of a

converging nozzle. Flow entering the nozzle greater than Mach 1, regardless of how much greater, will leave the nozzle at Mach 1. This means the flow is choked. The
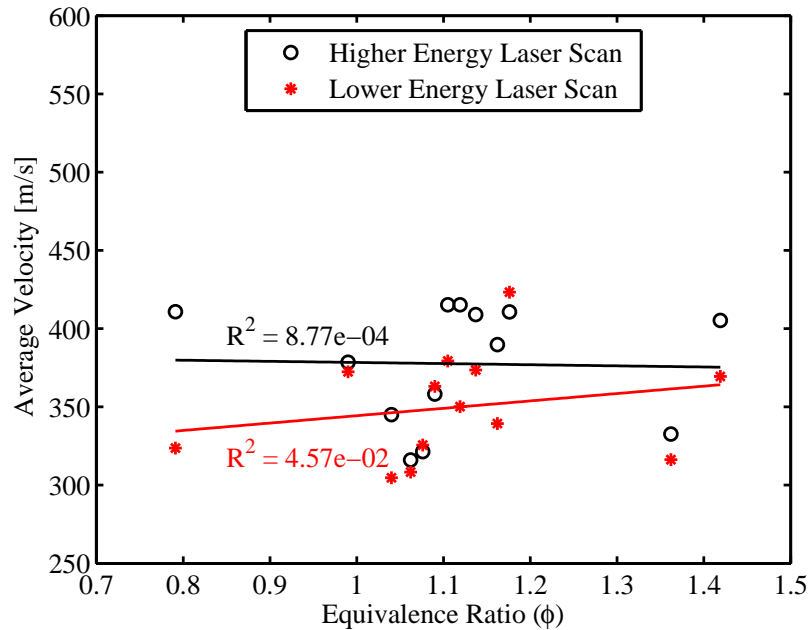

Figure 7.4: This figure depicts how the average steady state velocity changes with equivalence ratio. The two curves shown are both linear fits to the two sets of data.

velocity obtained from the high and low energy laser scans followed a similar trend. This can be more clearly seen by their corresponding fits in Figure 7.4. In many cases the velocity measurements made with the two lasers agreed fairly well, however, the higher energy laser tended to yield higher velocities than the lower energy laser. Ideally the velocities for each laser would be the same because they were taken during the same runs during the same time frames. The difference between the two values may arise from the difference in frequencies of the two lasers. The higher energy laser, when looking at the spectral lines on a wavenumber axis, is more sensitive to the Doppler shift than the lower energy laser. That is, the spectral lines observed with the higher energy laser shift more than the ones observed with the lower energy laser on a wavenumber axis. On a wavelength axis the effect is the opposite because of the

inverse relationship between wavenumbers and wavelengths. The larger shift is easier to detect and thus for the higher energy spectral lines, small changes have a smaller effect on the calculated velocity than they do with the lower energy spectral lines. This suggests that the higher energy laser scan points seen in Figure 7.4 are probably more accurate than those from the lower energy laser scan. Table 7.1 displays the data points calculated for the various equivalence ratios, along with the standard deviations.

7.3.2   *Temperature.*

Figure 7.5 shows two times series plots for both temperature and water concentration. The large spike in both temperature and concentration at the very beginning of both Figures 7.5a and 7.5b was partly due to decoupling of the lasers when the initial detonation propagated past the lasers. The small plateau in the temperature in Figure 7.5a near 1,500 Kelvin was believed to be a real temperature feature because the error in the simulated fits to the measured spectra in this region were comparable to the rest of the fits in the data set. This feature is also reflected in the water concentrations in Figure 7.5a. This plateau region can be seen in both the temperature and the concentration for various equivalence ratios, however, it was more prominent for the experiments with lower equivalence ratios. This can be seen in Appendix A.

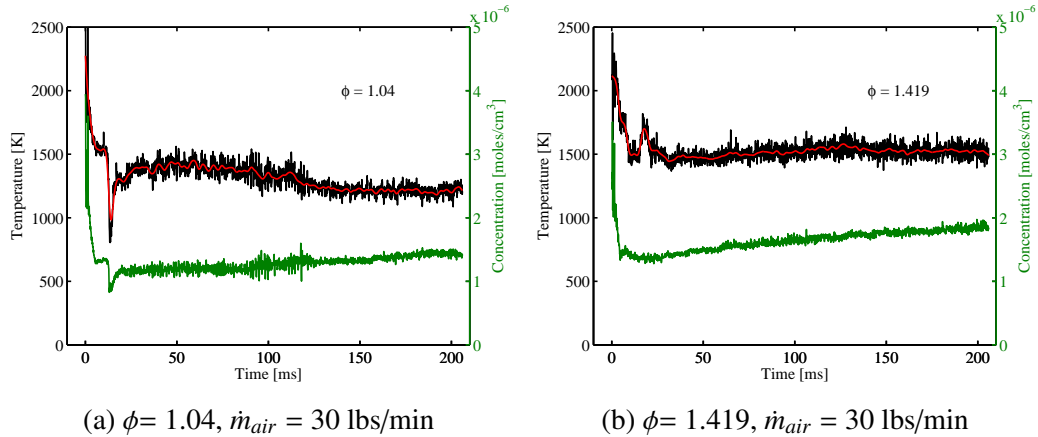(a) ϕ= 1.04, $\dot{m}_{air}$ = 30 lbs/min   (b) ϕ= 1.419, $\dot{m}_{air}$ = 30 lbs/min

Figure 7.5: This figure shows the temperature and water concentration time series results for the first 200 ms of RDE operation at two different equivalence ratios. The temperature curve was smoothed to produce the red curve to show the general trend of the data.

An interesting phenomenon occurs in both Figure 7.5a and Figure 7.5b. Near 10 ms in Figure 7.5a there is a sharp dip in temperature and concentration, and near 20 ms in Figure 7.5b there is a sharp rise in temperature (though not in concentration). In Appendix A the time series plots are ordered from low to high equivalence ratio. It can be seen that the sharp dip in the temperature transitions to a sharp rise in temperature as the equivalence ratio is increased. This transition occurred near an equivalence ratio of 1.16. The cause of this phenomenon was speculated to be the result of a manifold response to the initial detonation. At lower equivalence ratios the fuel flow rate was less than that of the higher equivalence ratios. It was believed that at the lower flow rates the flow was suppressed by the initial detonation, which caused a temporary drop in the equivalence ratio, resulting in lower temperatures. The suppression in the flow was reduced as the flow rate was increased until a neutral point was reached (near an equivalence ratio of 1.16). It was believed that as the flow rate was increased past the neutral point, there was a temporary sharp spike in the flow rate as the fuel valve was initially opened. This was believed to cause a temporarily elevated equivalence ratio, which caused the sharp rise in temperature. The effect of the fuel valve opening was

83

not seen in fuel flow rates below the neutral point because this effect was suppressed by the initial detonation.

Figure 7.6 shows the average temperature and water concentrations of the steady regions for various equivalence ratios. The temperature and concentration both increased with equivalence ratio. As can be seen by the R^2 values in the figure, the temperature had a stronger linear dependence on equivalence ratio. The two outliers, one for temperature near 1130 Kelvin and one for concentration near $1e^{-6}$ moles/cm^3, were not included in the linear fit. These two points were from the earliest dataset in the experiments and were believed to be low because the RDE may still have been cold.

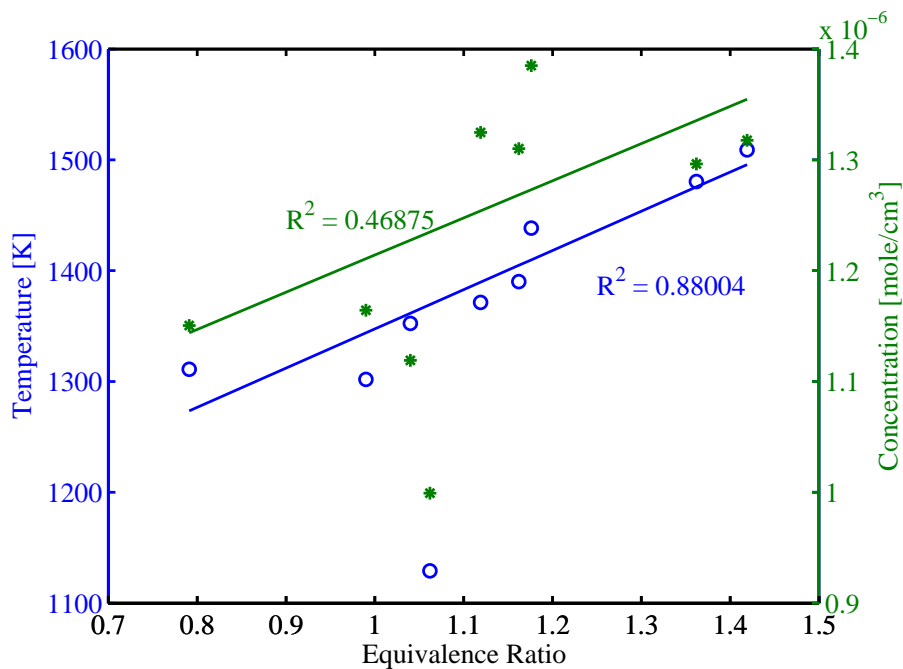Figure 7.6: This figure shows the average values of the temperatures and water concentrations in the steady state regions for the RDE exhaust at various equivalence ratios.

Normally, detonation and combustion reactions follow the trend seen in the Hencken burner results (Figure 5.2). The temperatures and concentrations tend to reach a maximum value near an equivalence ratio of 1.1. However, in Figure 7.6 this trend is

not followed. The RDE does not operate near adiabatic conditions, however, it can be useful to compare the results to the adiabatic conditions.

Figure 7.7a shows the measured temperatures of the RDE exhaust compared to the adiabatic detonation and deflagration temperatures. The measured temperatures were lower than the adiabatic temperatures. This was primarily due to heat loss to the walls of the RDE. Figure 7.7b shows the measured water concentration compared to the adiabatic water concentrations for detonations and deflagrations. At the lower equivalence ratio the concentration was below the adiabatic detonation values, however, for the higher equivalence ratios the measured values were higher than the adiabatic detonation values, and lower than the adiabatic deflagration values. This could be explained in two parts. First, the slightly lower concentrations at lower equivalence ratios could be caused by an incomplete detonation such that not all of the fuel was detonated. Second, at the higher equivalence ratios it is possible that a larger percent of the fuel was not detonated and was instead, combusted down stream of the detonation channel. This combination of detonation and deflagration would explain the rise in water concentration above the adiabatic detonation values (seen in Figure 7.7b). This would also explain why the temperature linearly increased with equivalence ratio instead of dropping off after an equivalence ratio of 1.1. If combustion occurred after the detonation channel than there would be a flame closer to the measurement location. This would reduce the amount of heat loss to the walls, and would raise the measured temperature.
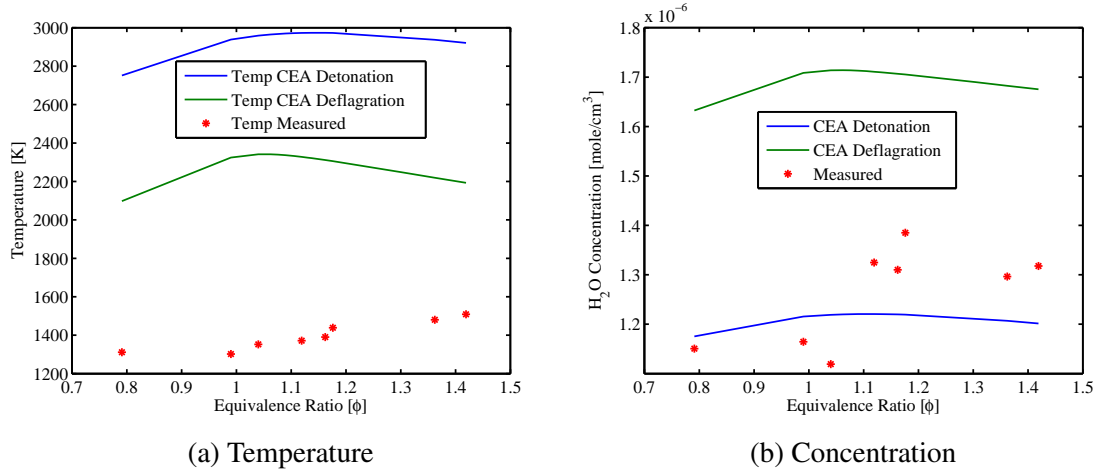
(a) Temperature (b) Concentration

Figure 7.7: This figure shows the average temperatures and water concentrations compared to the adiabatic detonation and deflagration values from NASA's CEA code [5].

Table 7.1 displays the average values of temperature, concentration, and velocity, along with the standard deviations of these parameters. The velocity was calculated for more equivalence ratios than the temperature and water concentration, as can be seen in the table. The standard deviations in the table do not necessarily reflect the standard deviations in the measuring capability of the TDM-TDLAS system, but instead represent the fluctuations in the operating conditions of the RDE.

Table 7.1: This table lists the results for the average temperature, water concentration, and velocity for the various equivalence ratios. All parameters were calculated after the steady state region was reached. The bar above the symbols indicates an averaged value and the subscript *std* indicates the standard deviation. *L* indicates the data are solely from the lower energy laser and the *H* is for the higher energy laser. ϕ stands for equivalence ratio, *T* for temperature, *C* for water concentration, and *V* stands for velocity.

ϕ	$\bar{T}$ [K]	T_{std} [K]	$\bar{C}[\frac{moles}{cm^3}]$	$C_{std}[\frac{moles}{cm^3}]$	$\bar{V}_L$ [m/s]	$V_{L_{std}}$[m/s]	$\bar{V}_H$ [m/s]	$V_{H_{std}}$ [m/s]
0.791	1,311	34.5	1.2E-6	3.6E-8	324	22.9	411	43.2
0.99	1,302	49.5	1.2E-6	6.2E-8	372	40.1	378	37.6
1.04	1,353	94.5	1.1E-6	1.1E-7	305	44.2	345	51.1
1.062	1,129	82.3	1.0E-6	1.0E-7	308	46.3	316.	49.1
1.076	-	-	-	-	326	50.6	321	64.0
1.09	-	-	-	-	363	44.3	358	44.5
1.105	-	-	-	-	379	52.0	415	52.3
1.119	1,371	53.6	1.3E-6	1.3E-7	350	46.7	415	64.2
1.137	-	-	-	-	373	48.8	409	68.5
1.162	1,390	82.7	1.3E-6	1.5E-7	339	44.5	390	54.2
1.176	1,438	56.6	1.4E-6	1.4E-7	423	63.3	411	76.2
1.362	1,480	43.5	1.3E-6	1.3E-7	316	44.1	333	52.3
1.419	1,509	51.2	1.3E-6	1.4E-7	369	54.3	405	70.4

VIII.   Conclusion

A graphical user interface was developed to analyze spectral data from a time-division multiplexed tunable diode laser absorption spectroscopy system. This GUI provides users with an interactive means to manipulate and process data. However, the program could be further optimized to greatly reduce the processing time.

The results from the Hencken burner for C_2H_4 matched NASA's CEA adiabatic temperatures very well at the lower temperatures; however, as the temperature increased, so did the disagreement with CEA calculations. A portion of this disagreement was believed to result from edge effects. This disagreement was reduced when an estimation of the edge effects was applied using PLIF images to scale the adiabatic temperatures. A portion of the increase in the disagreement with CEA with temperature was due to the increase in heat loss with temperature. The increased heat loss at higher temperatures caused the flame to diverge more from the adiabatic condition. The final reason for the disagreement was most likely from other non-uniformities throughout the flame causing the average temperature to be lower than the uniform flame temperatures.

The results for the CH_4 flame are found in Appendix B. These temperatures and concentrations diverged more from the adiabatic conditions than the C_2H_4 flame. This was believed to be caused by the larger non-uniformity throughout the flame. In future works PLIF images of the CH_4 flame could be used to determine the effect of the non-uniformities.

The program can handle many cases, however, further work is needed to analyze the high pressure and temperature conditions found within the detonation tube. Preliminary results show that there are two prominent features in the intensity profile

of the detonation, the first is the primary shock and combustion region, and the second larger feature is a reflected detonation wave off of the end wall of the detonation tube.

The results from the RDE system showed that the exhaust velocity reached a steady state condition rather quickly (between 10 and 50 ms). In the steady state region the velocity had an average near 360 m/s with a standard deviation of 50 m/s. The velocity of the exhaust gas was independent of the equivalence ratio. This was due to a converging nozzle upstream of the measurements. Further studies of the data must be performed to resolve the discrepancy between the velocity measurements taken with the two different laser diodes. Both the temperature and concentration exhibited a linearly increasing dependence on equivalence ratio. This was believed to be caused by incomplete detonations at higher equivalence ratios, which allowed for combustion to occur downstream the detonation channel. This combustion would have been closer to the test section which would have resulted in a rise in temperature for higher equivalence ratios as was seen in the data. The temperature ranged from 1,300 K to 1,500 K with standard deviations in the temperatures ranging from 30 to 90 K. The concentrations ranged from 1.0e-6 to 1.3e-6 moles/cm^3 with standard deviations ranging from 3.5e-8 to 1.5e-7 moles/cm^3.

Appendix A: RDE

This appendix contains additional time series results for the RDE. These results were obtained on the same RDE with same experimental setup as discussed in section 7.2. Hydrogen-air was used with an air mass flow rate of 30 lbs/min.
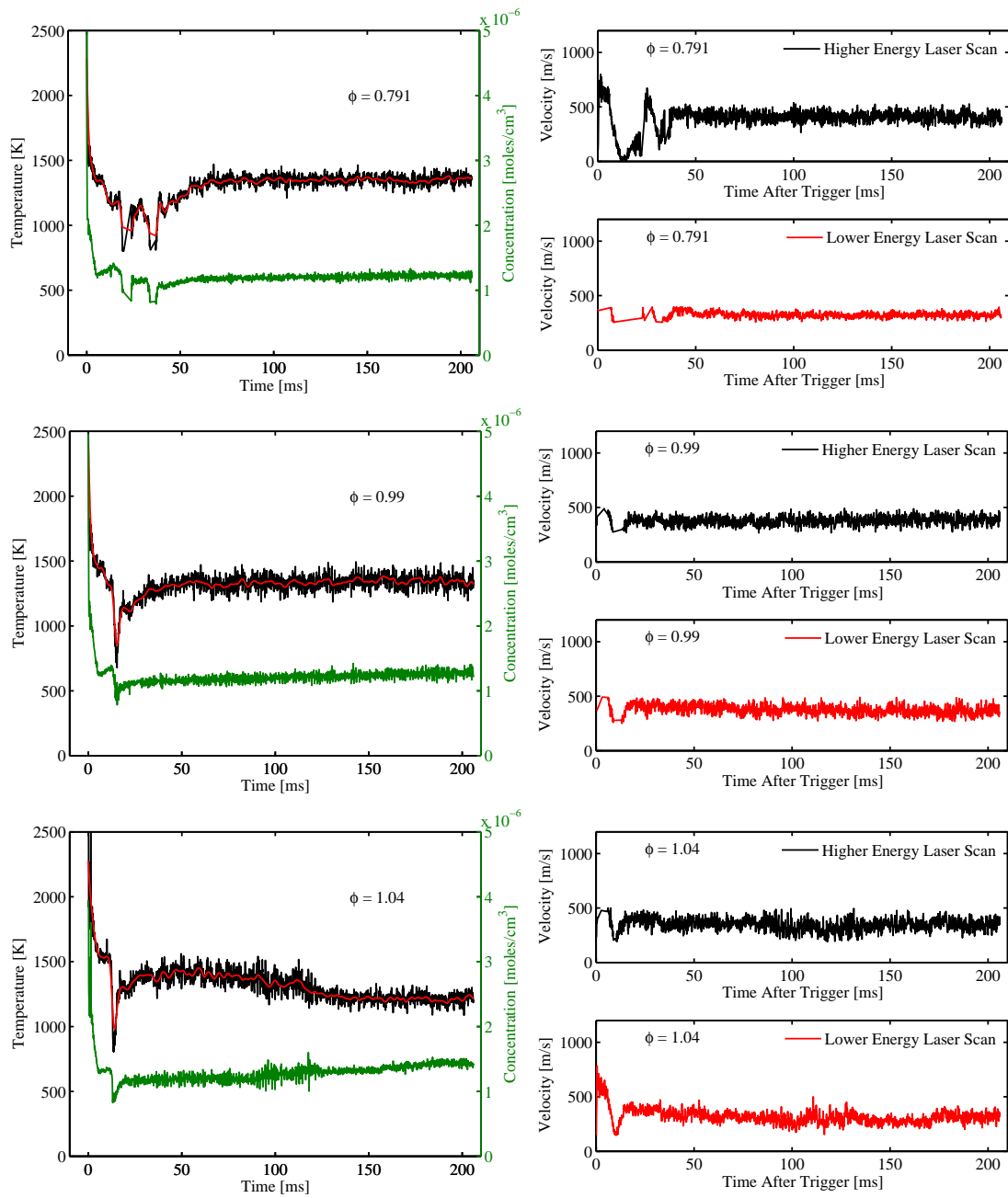
Figure A.1: The top two figures, equivalence ratio of 0.791, were deflagrations as opposed to detonations. The middle figures, equivalence ratio of 0.99, started as deflagrations and transitioned into detonations. This was determined by the sound of the RDE and a pressure probe in the detonation channel.
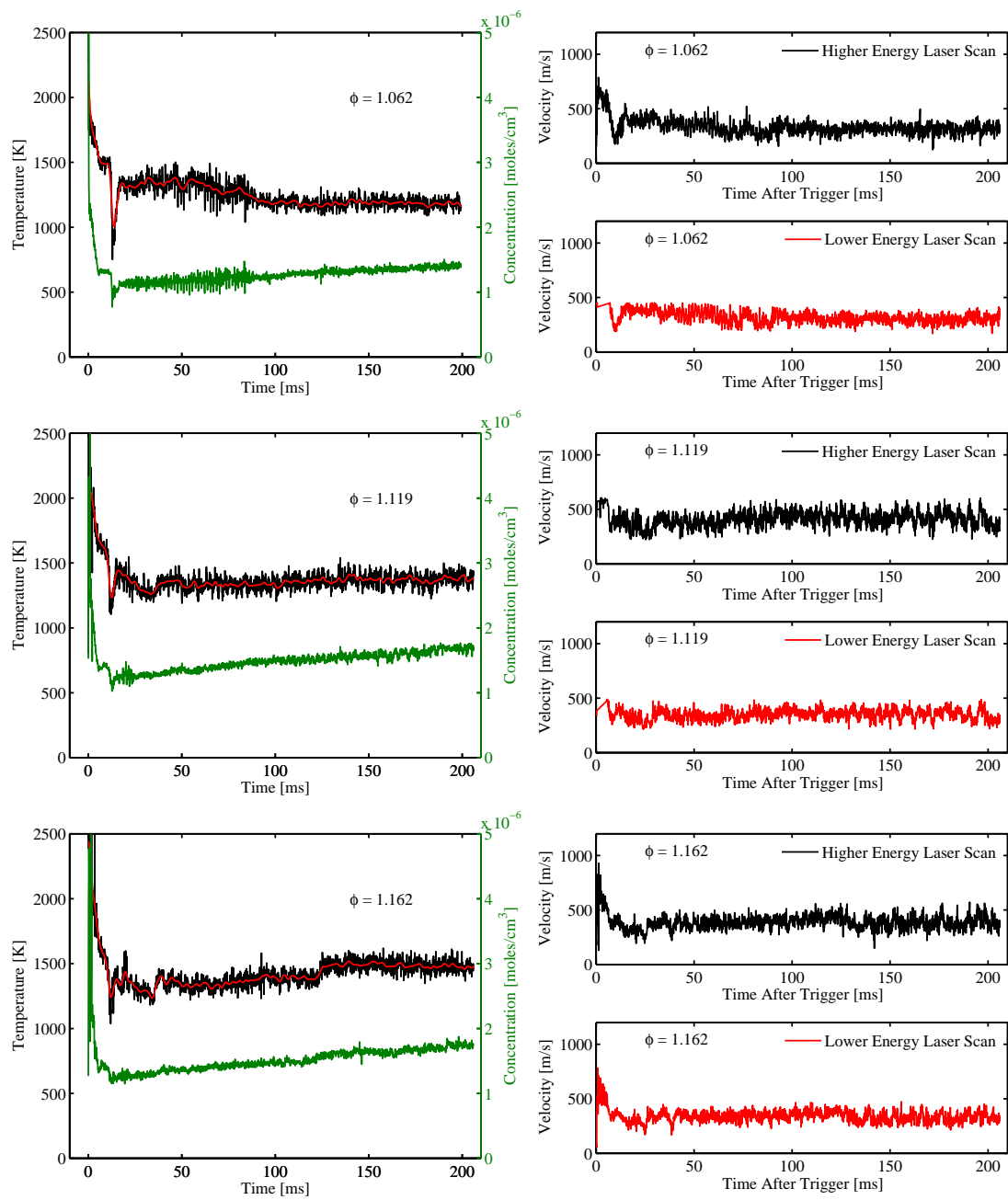
Figure A.2: The bottom temperature figure, equivalence ratio of 1.162, shows part of the transition between the dip in temperature at lower equivalence ratios, to the spike in temperature at higher equivalence ratios as discussed in section 7.3.2.
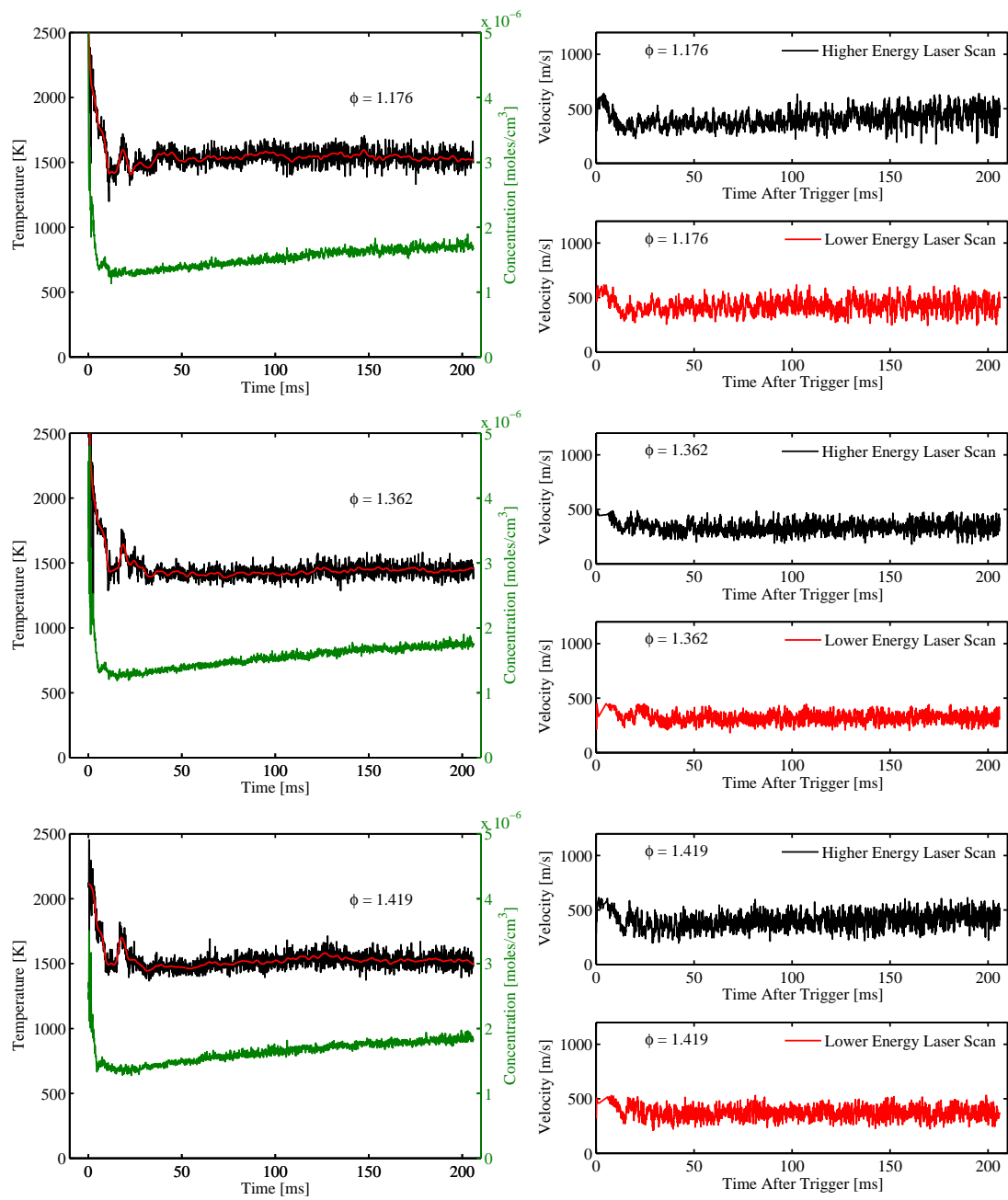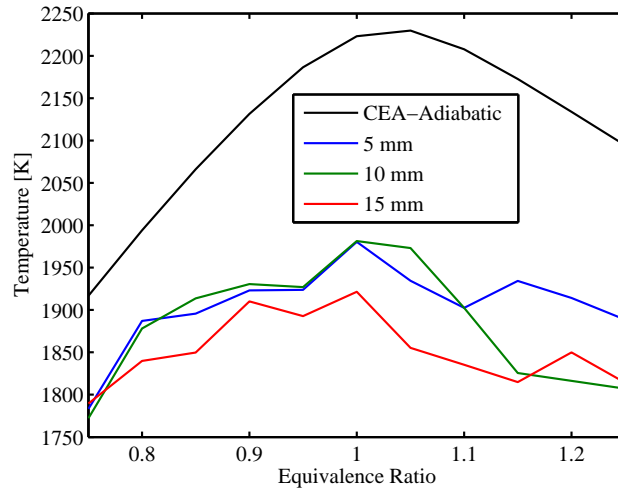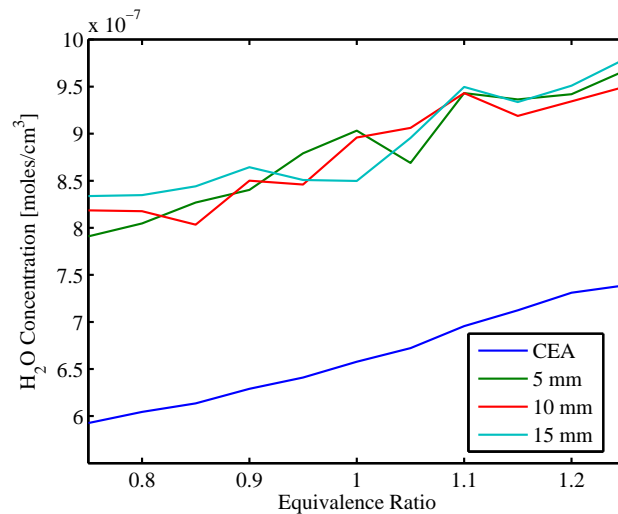
Figure A.3: In all of the time series plots, outliers in the steady state region of more than three standard deviations were removed. These were caused by decoupling of the lasers.

Appendix B: Hencken Burner CH$_4$

(a) Average CH$_4$ flame temperatures.

(b) Average CH$_4$ flame H$_2$O concentrations.

Figure B.1: The measured temperatures in Figure B.1a follow the same trend as the adiabatic temperature curve, however, they exhibit a large fluctuation from equivalence ratio to equivalence ratio, as opposed to being smoothed like the CEA calculated curve. These fluctuations are believed to cause instability in the CH$_4$ flame. Unlike the C$_2$H$_4$ flame which had a fairly uniform flame, the CH$_4$ flame had many small flamlets. In (b) the water concentrations are plotted for three different heights above the burner surface. These concentrations follow the same trend as the CEA calculated concentrations, however, unlike the case with C$_2$H$_4$ the measured concentration is larger than the adiabatic concentration. The cause of this is unknown and requires further investigation.

References

[1]   Basu, Saptarshi, Derek E. Lambe, and Ranganathan Kumar.   "Water vapor and carbon dioxide species measurements in narrow channels". *International Journal of Heat and Mass Transfer*, 53(4):703 – 714, 2010. URL http://www.sciencedirect.com/science/article/pii/S0017931009005626.

[2]   Bernath, Peter F. *Spectra of Atoms and Molecules*. Oxford University Press Inc., 198 Madison Avenue, New York, New York, 10016, second edition, 2005.

[3]   Caswell, Andrew W., Sukesh Roy, Xinliang An, Scott T. Sanders, Frederick R. Schauer, and James R. Gord. "Measurements of multiple gas parameters in a pulsed-detonation combustor using time-division-multiplexed Fourier-domain mode-locked lasers". *Appl. Opt.*, 52(12):2893–2904, Apr 2013. URL http://ao.osa.org/abstract.cfm?URI=ao-52-12-2893.

[4]   Demtröder, Wolfgang. *Laser Spectroscopy*. Springer, Germany, third edition, 2003.

[5]   Gordon, Sanford and Bonnie J. McBride. *Computer Program for Calculation of Complex Chemical Equilibrium Compositions and Applications*. 1311. National Aeronautics and Space Administration, Office of Management, Scientific and Technical Information Program, 1994.

[6]   Liepmann, H.W. and A. Roshko. *Elements of Gasdyanmics*. Dover Publications inc., Mineola, New York, 1985.

[7]   McClatchey, R.A., W.S. Benedict, S.A Clough, C.E. Burch, R.F. Calfee, K. Fox, L.S Rothman, and J.S. Garing. "AFCRL Atmospheric Absorption Line Parameters Compilation". *Environmental Research Papers*, (434):1 – 7, 1973. Original HITRAN Report.

[8]   Meyer, Terrence R., Sukesh Roy, Viswanath R. Katta Robert P. Lucht Thomas N. Anderson, Joseph D. Miller, and James R. Gord. "Measurements of OH mole fraction and temperature up to 20 kHz by using a diode-laser based UV absorption sensor". *Applied Optics*, 44:6,729–6,740, 2005.

[9]   Naples, Andrew, John Hoke, James Karnesky, and Fredrick Schauer. "Flow Field Characterization of a Rotating Detonation Engine". *51st AIAA Aerospace Sciences Meeting including the New Horizons Forum and Aerospace Exposition*. Aerospace Sciences Meetings, American Institute of Aeronautics and Astronautics, 2013.

[10] Naples, Andy, John Hoke, Nick Debarmore, Scott Theuerkauf, Rod Fievisohn, Rachel Russo, and Fred Schauer. "Characterization of a Rotating Detonation Engine Flowfield". *Proceedings of the COMBEX-2013 Conference*. March 2013.

[11] Nordeen, Craig A., Douglas Shwer, Fredrick Schauer, John Hoke, Baki Cetegen, and Thomas Barber. "Energy Transfer in a Rotating Detonation Engine". *47th AIAA/ASME/SAE/ASEE Joint Propulsion Conference & Exhibit*. Joint Propulsion Conferences, American Institute of Aeronautics and Astronautics, 2011.

[12] Ren, W., A. Farooq, D.F. Davidson, and R.K. Hanson. "CO concentration and temperature sensor for combustion gases using quantum-cascade laser absorption near 4.7μm". *Applied Physics B*, 107(3):849–860, 2012. ISSN 0946-2171. URL http://dx.doi.org/10.1007/s00340-012-5046-1.

[13] Sauer, Timothy. *Numerical Analysis*. Pearson Addison Wesley, Boston, second edition, 2012.

[14] Schwer, D.A. and K. Kailasanath. "Rotating Detonation-Wave Engines". *Naval Research Reviews*, 2011.

[15] Schwer, Douglas and Kailas Kailasanath. "Numerical investigation of the physics of rotating-detonation-engines". *Proceedings of the Combustion Institute*, 33(2):2195 – 2202, 2011. ISSN 1540-7489. URL http://www.sciencedirect.com/science/article/pii/S1540748910003159.

[16] Theuerkauf, Scott W. *Heat Exchanger Design and Testing for a 6-inch Rotating Detonation Engine*. Master's thesis, Air Force Institute of Technology, Wright-Patterson Air Force Base, Ohio, 2013.

[17] Turns, Stephen R. *An Introduction to Combustion, Concepts and Applications*. WCB/McGraw-Hill, Boston, 2000.

[18] Varshni, Y.P. "Temperature dependence of the Energy Gap in Semiconductors". *Physica*, 34(1):149 – 154, 1967. URL http://www.sciencedirect.com/science/article/pii/0031891467900626.

[19] Whiting, E. E. "An Empirical Approximation to the Voigt Profile". *Journal of Quantitative Spectroscopy and Radiative Transfer*, 8(6):1379 – 1384, 1968. ISSN 0022-4073. URL http://www.sciencedirect.com/science/article/pii/0022407368900812.

[20] Whitney, Jean, Andrew Caswell, Suhesh Roy, James R Gord, and Scott T. Sanders. "Tunable 2-VCSEL system applied for H_2O vapor absorption thermometry in rotating detonation engine exhaust". (To be published).

REPORT DOCUMENTATION PAGE

Form Approved
OMB No. 0704–0188

1. REPORT DATE *(DD–MM–YYYY)*	2. REPORT TYPE	3. DATES COVERED *(From — To)*
27–03–2014	Master's Thesis	Oct 2013–Mar 2014

4. TITLE AND SUBTITLE	5a. CONTRACT NUMBER
Utilizing Near-IR Tunable Laser Absorption Spectroscopy to Study Detonation and Combustion Systems	5b. GRANT NUMBER
	5c. PROGRAM ELEMENT NUMBER
6. AUTHOR(S)	5d. PROJECT NUMBER
McGahan, Christopher J., Second Lieutenant, USAF	5e. TASK NUMBER
	5f. WORK UNIT NUMBER

7. PERFORMING ORGANIZATION NAME(S) AND ADDRESS(ES)	8. PERFORMING ORGANIZATION REPORT NUMBER
Air Force Institute of Technology Graduate School of Engineering and Management (AFIT/EN) 2950 Hobson Way WPAFB, OH 45433-7765	AFIT-ENP-14-M-22

9. SPONSORING / MONITORING AGENCY NAME(S) AND ADDRESS(ES)	10. SPONSOR/MONITOR'S ACRONYM(S)
Intentionally Left Blank	11. SPONSOR/MONITOR'S REPORT NUMBER(S)

12. DISTRIBUTION / AVAILABILITY STATEMENT

DISTRIBUTION STATEMENT A. APPROVED FOR PUBLIC RELEASE; DISTRIBUTION UNLIMITED.

13. SUPPLEMENTARY NOTES

This work is declared a work of the U.S. Government and is not subject to copyright protection in the United States.

14. ABSTRACT

A Hencken burner, RDE, and a detonation tube were studied using a TDM-TDLAS system to measure water absorption features over two spectral regions (7,435 to 7,442 cm^{-1} and 7,465 to 7,471 cm^{-1}) near 1.3 μm. These absorption features were fit with simulated spectra using data from the HITEMP database to obtain temperatures and water concentrations for the three systems. Velocity was calculated for the RDE system using the Doppler shift of the spectral lines. To perform the calculations necessary to obtain these results (temperature, concentration, and velocity) a GUI was developed with supporting code. A Hencken burner flame was studied at three different heights above the burner surface, for two different fuels; ethylene (C_2H_4) and methane (CH_4), both at various equivalence ratios. The C_2H_4 Hencken burner temperatures matched fairly well with the adiabatic temperatures once edge effects were taken into account, however, the CH_4 flame did not match as well. The exhaust of the RDE was studied at various equivalence ratios using a hydrogen-air mixture (H_2-air). The exhaust temperatures were found to linearly increase with equivalence ratio, from 1,300 K ($\phi \approx 1$) to 1,500 K ($\phi \approx 1.4$) and fluctuated with a standard deviation of approximately 50 K. The exhaust velocities of the RDE were found to be independent of equivalence ratio with an average value of 360 m/s and a standard deviation of 50 m/s. A detonation tube was studied at various equivalence ratios and initial pressures, also using an H_2-air mixture. Preliminary results are presented for the detonation tube, however, further work in that area is required.

15. SUBJECT TERMS

TDLAS, rotating detonation engine, Hencken burner

16. SECURITY CLASSIFICATION OF:			17. LIMITATION OF ABSTRACT	18. NUMBER OF PAGES	19a. NAME OF RESPONSIBLE PERSON
a. REPORT	b. ABSTRACT	c. THIS PAGE			Col. Brian A. Tom, AFIT/ENP
U	U	U	UU	114	19b. TELEPHONE NUMBER *(include area code)* (937) 255-6565x7112 Brian.Tom@afit.edu

Standard Form 298 (Rev. 8–98)
Prescribed by ANSI Std. Z39.18